THE GEOLOGICAL SOCIETY
OF AMERICA®

Grenvillean evolution of the Beishan Orogen, NW China: Implications for development of an active Rodinian margin

Jérémie Soldner[1,2,†], Chao Yuan[1,§], Karel Schulmann[3,4], Pavla Štípská[3,4], Yingde Jiang[1], Yunying Zhang[5], and Xinyu Wang[1]

[1]*State Key Laboratory of Isotope Geochronology and Geochemistry, Guangzhou Institute of Geochemistry, Chinese Academy of Sciences, Guangzhou 510640, China*
[2]*University of Chinese Academy of Sciences, Beijing 10069, China*
[3]*Institut de Physique du Globe de Strasbourg, UMR 7516, University of Strasbourg/School and Observatory of Earth Sciences, Centre National de la Recherche Scientifique; 1 rue Blessig, F 67084 Strasbourg, France*
[4]*Centre of Lithospheric Research, Czech Geological Survey, Klárov 3,118 21 Praha 1, Czech Republic*
[5]*Department of Earth Sciences, The University of Hong Kong, Pokfulam Road, Hong Kong, China*

ABSTRACT

New geochemical and geochronological data are used to characterize the geodynamic setting of metasediments, felsic orthogneisses, and eclogite and amphibolite lenses forming the Beishan complex, NW China, at the southern part of the Central Asian Orogenic Belt. The metasediments correspond compositionally to immature greywackes receiving detritus from a heterogeneous source involving a magmatic arc and a Precambrian continental crust. Metagranitoids, represented by felsic orthogneisses, show both composition of greywacke-derived granitic melt with incompatible trace element patterns similar to the host metasediments. The eclogite lenses are characterized by high Nb contents (5.34–27.3 ppm), high $(Nb/La)_N$ (>1), and low Zr/Nb ratios (<4.5), which together with variable and negative whole-rock $\varepsilon_{Nd}(t)$ (–4.3 to –10.3) and zircon $\varepsilon_{Hf}(t)$ (–5.0 to + 2.3) values indicate an origin of enriched mantle source as commonly manifested by back-arc basalts at stretched continental margins. Combined with monazite rare earth element analysis, the in situ monazite U-Pb dating of metagraywacke (880.7 ± 7.9) suggests garnet growth during a high-temperature (HT) metamorphic event. Together with U-Pb dating of zircon metamorphic rims in amphibolite (910.9 ± 3.0 Ma), this indicates that the whole crustal edifice underwent a Grenvillian-age metamorphic event. The protolith ages of the eclogite (889.3 ± 4.8 Ma) and orthogneiss (867.5 ± 1.9 Ma) suggest that basalt underplating and sediment melting were nearly coeval with this HT metamorphism. Altogether, the new data allow placing the Beishan Orogen into a Grenvillean geodynamic scenario where: (1) The late Mesoproterozoic to early Neoproterozoic was marked by deposition of the greywacke sequence coeval with formation of an early arc. (2) Subsequently, an asthenospheric upwelling generated basaltic magma underneath the thinned subcontinental mantle lithosphere that was responsible for HT metamorphism, melting of the back-arc basin greywackes and intrusion of granitic magmas. These events correspond to a Peri-Rodinian supra-subduction system that differs substantially from the Neoproterozoic ophiolite sequences described in the Mongolian part of the Central Asian Orogenic Belt, thus indicating important lateral variability of supra-subduction processes along the Rodinian margin.

INTRODUCTION

Recent advances in geochronology of the Central Asian Orogenic Belt (CAOB) indicate a widespread presence of Neoproterozoic (Grenvillian age—1000–850 Ma) rocks associated with the Peri-Siberian and Mongolian microcontinents and ophiolites in the north (Khain et al., 2003; Rojas-Agramonte et al., 2011). In the south, Neoproterozoic (Grenvillean age—1050–900 Ma) rocks are associated with the Tarim Precambrian microcontinent (Rojas-Agramonte et al., 2011). In Mongolia, these sequences are represented by gabbros, tonalities (973–941 Ma; Buriánek et al., 2017), and andesitic volcanics (811–787 Ma; Bold et al., 2016b). These rocks were interpreted as an arc established on an early Proterozoic continental crust (Bold et al., 2016b; Buriánek et al., 2017). On the other hand, Peri-Rodinian oceanic gabbros (Erdene Uul at ca. 973 Ma; Buriánek et al., 2017) or even mature intraoceanic arc magmatic associations (Dunzhugur arc dated at 1000–800 Ma, Kuzmichev et al., 2001; Kuzmichev and Larionov, 2011), such as the Nyur ophiolite of the Baikal-Muya belt (1035 Ma) or the Arz ophiolite (1017 Ma) indicate development of supra-subduction back-arc and arc sequences off the southern margin of the Siberia craton (Khain et al., 2003). All of these supra-subduction ophiolites were obducted over the Siberian margin or the Mongolian microcontinents during subsequent Neoproterozoic accretionary events (Khain et al., 2003; Buriánek et al., 2017). In the south, the Tarim microcontinent and the Beishan Orogen farther east also show important Neoproterozoic tectonothermal activity associated with magmatism and metamorphism (Ge et al., 2014; Liu et al., 2015). The northern margin of the Tarim block shows intrusion of granodiorites and tonalities into the Paleoproterozoic basement, which was interpreted as formation of a continental arc at ca. 830–800 Ma (Ge et al., 2014). Likewise, the Beishan Orogen shows the presence of orthogneiss bodies (1014–871 Ma) and paragneisses (1040–910 Ma) that were also interpreted to form at an active margin setting (Liu et al., 2015). This magmatic event was associated with medium pressure granulite facies metamorphism in the Tarim block and the formation of garnet-bearing amphibolites located southeast of the Tarim craton that were interpreted to reflect high-temperature (HT) accretion

†jeremie.soldner@gmail.com.
§Corresponding author: yuanchao@gig.ac.cn.

GSA Bulletin; July/August 2020; v. 132; no. 7/8; p. 1657–1680; https://doi.org/10.1130/B35404.1; 15 figures; 3 tables; Data Repository item 2020035.
published online 5 December 2019

in the region (Song et al., 2012; Ge et al., 2016). Altogether, the Tarim block and the Beishan Orogen 900–800 Ma magmatic and metamorphic associations were interpreted to reflect the main Peri-Rodinian accretion event (Song et al., 2012; Ge et al., 2016; Zhao et al., 2018).

The Beishan orthogneisses and metasediments in the Gubaoquan area, NW China, are associated with the eclogites having mid-ocean ridge basalt(MORB)-type chemistry and formed during a high-pressure (HP) event at 465–467 Ma (Yang et al., 2006; Liu et al., 2011). Based on these findings, Qu et al. (2011) interpreted the origin of these eclogites as products of early Palaeozoic subduction of Paleoasian oceanic crust that were later incorporated into continental crust. However, the protolith ages (860–886 Ma) of the eclogite have been recently reinterpreted as indicating that these rocks may have formed as an integral part of a Neoproterozoic crustal edifice (Saktura et al., 2017).

To solve the problem of the origin of the eclogites, orthogneisses, and metasediments in the Beishan Orogen we use whole rock geochemistry, isotope data, zircon geochronology, and Hf isotope systematics to constrain the nature of the metabasites and associated gneissic host rocks. We argue that the whole system represents a unique crustal segment formed by Grenvillean recycling of an old continental crust. The lower crust was formed by melting of a continental mantle associated with incursion of asthenospheric melts. In this model, the freshly deposited sediments were metamorphosed and partially molten to generate arc-like granitoids forming a middle crust. The geodynamic position of the whole system thus corresponds to Pacific type back-arc system, where mafic rocks represent part of the basaltic underplate and the orthogneiss-paragneiss association results from recycling of the sedimentary back-arc edifice. During, the early Paleozoic orogeny, it was the autochthonous mafic lower crust that reached eclogite-facies conditions and was later incorporated into middle crust during intracontinental collision (P. Štípská personal commun., 2019).

GEOLOGICAL SETTING

The Central Asian Orogenic Belt (CAOB) is bordered by the Siberian and East European cratons to the north and the Tarim and North China cratons to the south (Şengör et al., 1993; Jahn et al., 2004). The Beishan Orogen is located in the southern part of the CAOB, connecting the South Tianshan suture in the west and the Solonker suture in the east, and records the amalgamation of the Mongolian collage with the Tarim-North China cratons in the south (Xiao et al., 2018; Fig. 1A). It is bounded by the Hanshan microcontinent to the north, and the Dunhuang block to the south, which is considered either as the eastern extension of the Tarim craton or as a typical tectonic-metamorphic mélange consisting of eclogite, mafic granulite, and amphibolite (Wang et al., 2017). It was suggested that the Beishan Orogen is formed by polyphase accretion and amalgamation of magmatic arcs and microcontinents, separated by several ophiolitic belts (Zuo et al., 1991; Xiao et al., 2010). The Beishan Orogen is characterized by medium- to high-grade metamorphic rocks that are developed in all the tectonic units and are referred to as the "Beishan complex" (BGMRG, 1989; Zuo et al., 1991; Mei et al., 1998b; Xiao et al., 2010). In contrast to the above referred works, recent studies suggest that the whole Beishan Orogen can be regarded as a single continental terrane formed as early as the Paleoproterozoic, which is based on Hf model age peaks at ca. 1.0–0.8 Ga and 2.0–1.8 (He et al., 2018b).

In the studied area located in the southern part of the Beishan Orogen, the rocks from the Beishan complex are composed of medium- to high-grade granitic gneisses, migmatites, amphibolites, and micaschists (Xiao et al., 2010; Song et al., 2016; Zong et al., 2017; Zheng et al., 2018), and is also the host of several eclogite lenses (Mei et al., 1998b; Yang et al., 2006; Liu et al., 2011; Qu et al., 2011). The eclogite peak and retrograde metamorphism has been constrained at 15.5–18 kbar and 700–800 °C and 10–14 kbar and 650–750 °C using Grt-Cpx and Grt-Hbl geothermobarometers (Mei et al., 1998b; Qu et al., 2011). Zircon U-Pb dating has constrained the protolith age of the granitic gneisses to be ca. 871–1040 Ma. The geochemical signatures and zircon $\varepsilon_{Hf}(t)$ values of the granitic gneisses indicate involvement of an old crustal component and therefore the rocks have been interpreted as formed in an Andean-type continental margin magmatic arc (Ye et al., 2013; Liu et al., 2015; Yuan et al., 2015; He et al., 2018b). The protolith of the eclogite has been dated at 860–886 Ma whereas the eclogite-facies metamorphism has been constrained at 465–467 Ma using in situ zircon U-Pb dating method (Yang et al., 2006; Liu et al., 2011, Qu et al., 2011; Saktura et al., 2017). Chondrite-normalized rare earth element (REE) and primitive mantle normalized trace element patterns and $\varepsilon_{Nd}(t)$ values (+6.4 to –1.6) show enriched (E)- and normal (N)-MORB type features for the eclogite. Thus, the eclogites were ascribed either to seamount and oceanic crust (Qu et al., 2011) or to mafic dykes intruded in a continental crust (Saktura et al., 2017). The region referred to as the Dundunshan arc (Fig. 1B) is also composed of Paleozoic clastic rocks and carbonates, Neoproterozoic granitic rocks of the Beishan complex (Zuo et al., 1990; Fig. 1B), Late Ordovician to Devonian volcanic rocks such as Nb-enriched basalts, andesites, and tuffs (e.g.; Mao et al., 2012a; Guo et al., 2014) as well as 442–217 Ma granitic intrusions (e.g., Zhao et al., 2007; Li et al., 2012, 2013; Zhang et al., 2012).

GEOLOGY OF THE STUDIED AREA

In the studied area, large eclogite boudins (up to 300 m long and 100 m wide) with eclogite rims retrogressed at amphibolite facies conditions and small amphibolite lenses occur within orthogneiss and metasediments (Figs. 2 and 3A–3C). Eclogite occurs as massive and isotropic rocks and do not exhibit any fabric, except at rims of large boudins affected by amphibolite-facies retrogression. The structural relations between the eclogite and the surrounding rocks indicate the presence of a regional foliation S3 at the eclogite rims, and well preserved in metasediments. This N-S–trending, steep schistosity is reworked by open to isoclinal F3 folds associated with development of a penetrative S3 axial planar cleavage steeply dipping to the N-NE (Figs. 2 and 3D). Leucogranitic veins intrude the metabasite boudins and the gneisses, and are affected by S3 in the gneisses (Fig. 3B). All the fabrics and leucogranitic veins are crosscut by metric subvertical E-W and ENE-WSE–striking doleritic dikes (Figs. 3A and 3B).

Petro-structural analyses (P. Štípská personal commun., 2019) shows that eclogite preserves the Grt-Cpx-Hbl-Qz-Rt mineral assemblages M1 corresponding to peak metamorphic conditions of 16–17 kbar and ~750 °C (Mei al., 1999; Qu et al., 2011) followed by D2 retrogression characterized by clinopyroxene-plagioclase symplectites. The metapelite shows Grt-Ky-Bt-Pl-Qz-Rt syn-S2 assemblage formed at peak metamorphic conditions of 8–8.5 kbar and ~640 °C. Late S3 fabric at the margins of the eclogite lenses is related to formation of recrystallized amphibole-bearing matrix, while in the metapelite the S3 is marked by andalusite-, sillimanite-, biotite-, and chlorite-bearing fabric formed on decompression down to 3–4 kbar and 550–575 °C.

SAMPLE PETROGRAPHY

The petrography of eclogite, amphibolite, orthogneiss, and metasediments is shown in Figure 3. Mineral abbreviations are after Whitney and Evans (2010). The massive coarse- to medium-grained eclogites are characterized by the Grt-Cpx-Pl-Amp-Qz-Rt-Ilm mineral assemblage. The prograde metamorphic mineral assemblage preserved as inclusions in garnet is Cpx-Hbl-Pl-Qz-Ilm. Relicts of the HP eclogitic

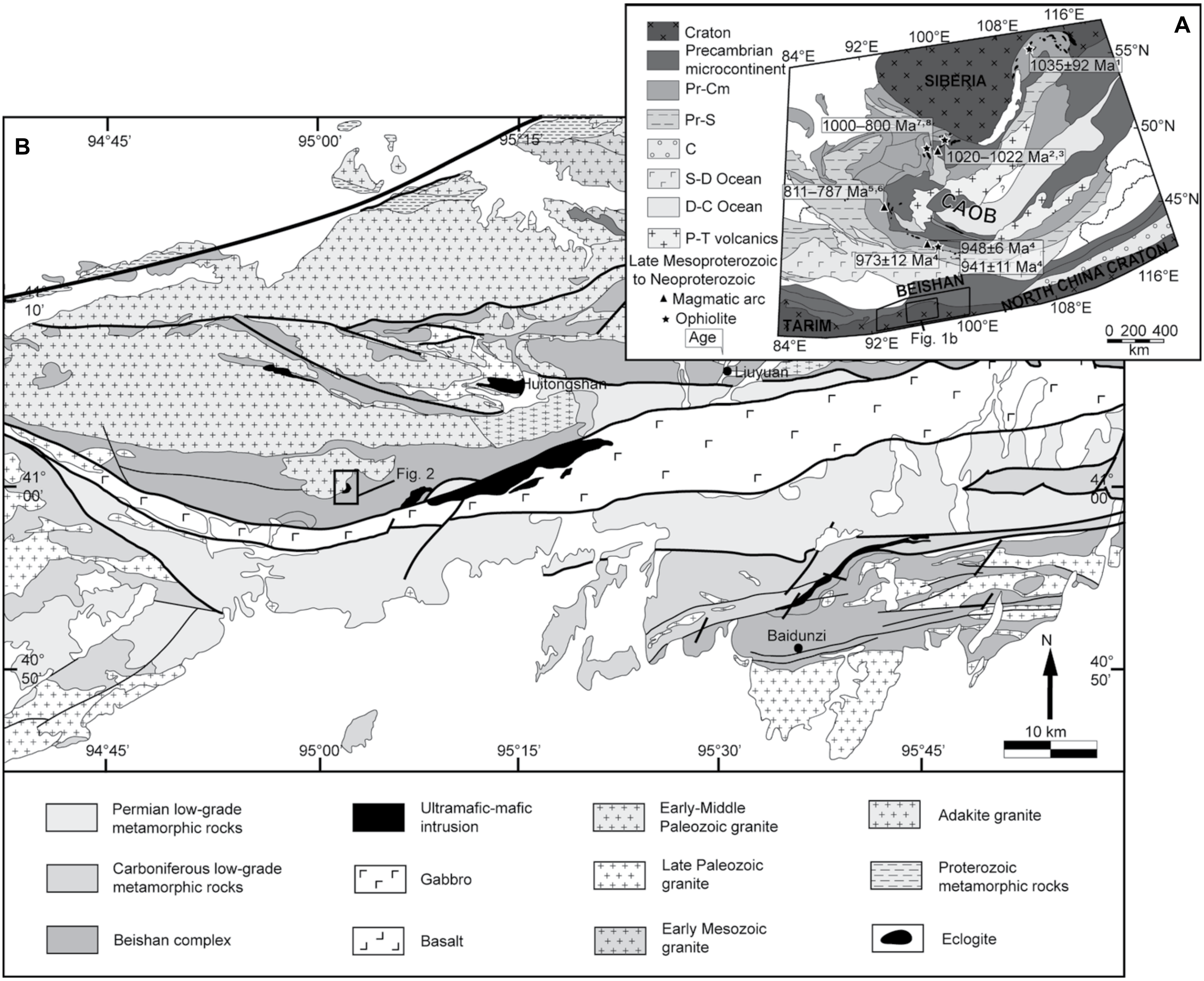

Figure 1. (A) Simplified map of the Central Asian Orogenic Belt (modified from Wilhem et al. (2012) and Buriánek et al. (2017). Ages of late Mesoproterozoic to Neoproterozoic arcs and ophiolites are from [(1)]Ritsk et al. (1999a), [(2,3)]Khain et al. (2002, 2003), [(4)]Buriánek et al. (2017), [(5,6)]Bold et al. (2016a, 2016b), and [(7,8)]Kuzmichev et al. (2001, 2005). The maps show the position of the Beishan Orogen (NW China), the principal sutures and the principal tectonic zones according to Zonenshain (1973) and Kröner et al. (2010). (B) Simplified geological map of the Shuangyingshan (or the Huaniushan arc) area with the main stratigraphic units and intrusive rocks (modified after BGMRG, 1989; Zuo et al., 1990; Nie et al., 2002a; Mao et al., 2012a). Pr-Cm—Proterozoic-Cambrian; Pr-S—Proterozoic-Silurian; C—Carboniferous; S-D—Silurian-Devonian; D-C—Devonian-Carboniferous; P-T—Permian-Triassic.

peak-metamorphism occur in the matrix in the form of the Grt-Cpx-Hbl-Qz-Rt mineral assemblage. The Grt-Cpx-Hbl-Pl-Qz-Rt mineral assemblage corresponds to early retrogression during exhumation and is characterized by development of clinopyroxene-plagioclase symplectites (symp I) along clinopyroxene cleavages and amphibole-plagioclase symplectites (symp II) along the boundaries of clinopyroxene (Fig. 3E). Further retrogression stages are depicted by amphibole-plagioclase kelyphites around garnet and replacement of rutile by ilmenite. In the rims of the eclogite, retrogression is characterized by recrystallization of matrix amphibole and corresponds to the Grt-Amp-Pl-Chl-Qz-Kfs-Ilm mineral assemblage. Amphibolite occurring as small boudins is isotropic and characterized by the mineral assemblages of Amp-Pl-Qz-Ilm and Amp-Pl-Qz-Bt-Ilm (Fig. 3F).

Orthogneiss is characterized by monomineralic recrystallized quartz ribbons alternating with biotite- and muscovite-rich layers around K-feldspar and plagioclase augen porphyroclasts (Figs. 3D and 3G). Mineral assemblages observed in the orthogneiss are Kfs-Pl-Qz-Bt-Ms-Chl and Kfs-Pl-Qz-Bt-Chl. K-feldspar and plagioclase augen underwent moderate sericitized during late D3 retrogression (Fig. 3G). Fractured garnet occurs locally in the matrix. Small monazite (<50 µm) and larger zircon (50–100 µm) grains are enclosed in feldspar augen, quartz ribbons or are present in the matrix.

The metasediments are characterized by monomineralic ribbons of recrystallized quartz alternating with biotite–muscovite-rich layers.

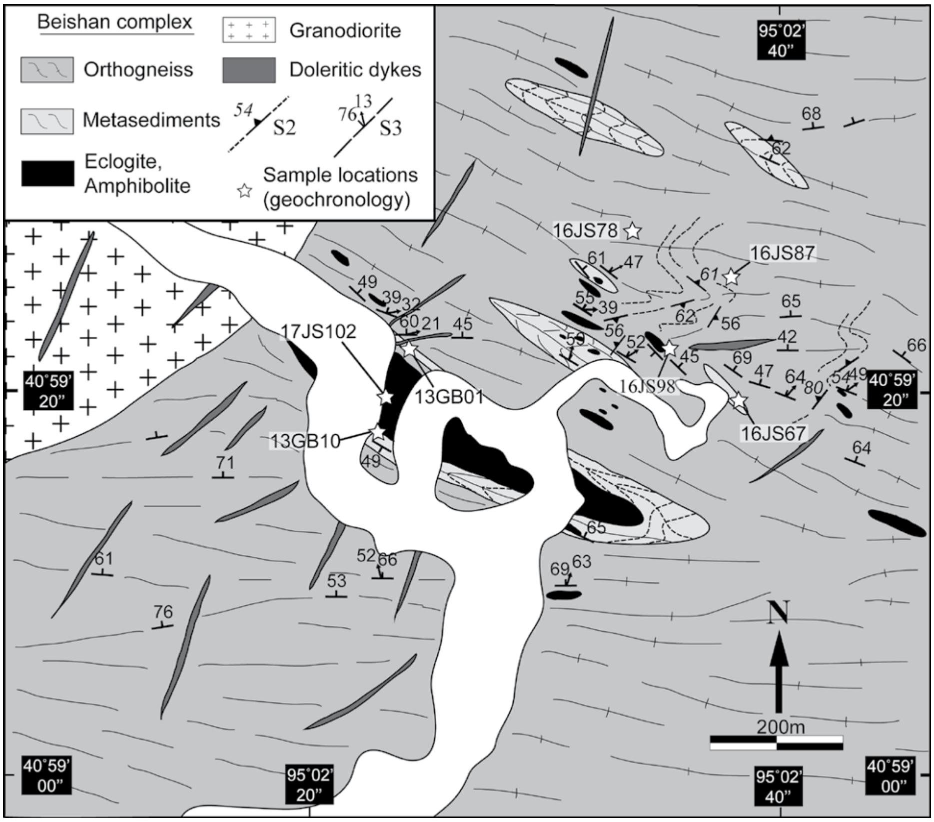

Figure 2. Geological map of the Gubaoquan area located in the southern Beishan complex, NW China. Locations of the samples for petro-structural and geochronological analysis are indicated.

Most metasediments have Grt-Bt-Ms-Pl-Qz-Chl-Ilm and Grt-Amp-Bt-Ms-Pl-Qz-Chl-Ilm mineral assemblages. In Al-rich metasediments, garnet, plagioclase, staurolite, kyanite, andalusite, and sillimanite occur locally in mica-rich layers (Fig. 3H). Garnet is either subhedral to anhedral, and commonly fractured. Kyanite and staurolite porphyroclasts occur within the matrix or are included in plagioclase and andalusite. The S3 foliation is defined by oriented biotite and muscovite and sometimes by sillimanite in andalusite- and plagioclase-rich layers (Fig. 3H). Chlorite and biotite in pressure shadows around andalusite and plagioclase indicate that the S3 deformation continued after andalusite growth at greenschist facies conditions (Fig. 3H). Small- to large monazite grains (<50–100 µm) occur as inclusions in garnet, biotite, plagioclase, and in quartz ribbons and the matrix. Most samples had experienced retrogression to variable degrees, characterized by chlorite, chlorite-muscovite aggregates, and fine-grained muscovite.

ANALYTICAL METHODS

Zircon trace element analysis and U-Pb dating were performed using laser ablation–inductively coupled plasma–mass spectrometry at the Key Laboratory of Mineralogy and Metallogeny (KLaBMM) and the State Key Laboratory of Isotope Geochemistry (SKLaBIG) at the Guangzhou Institute of Geochemistry Chinese Academy of Sciences (GIGCAS). In situ monazite U-Th-Pb and REE data were acquired at the State Key Laboratory of Geological Processes and Mineral Resources, China University of Geosciences, Wuhan. Whole-rock major and trace element chemistry, Sr-Nd isotopic analysis and cathodoluminescence (CL) images of zircon were done at the SKLaBIG at GIGCAS. Monazite compositional mapping and mineral analysis were carried out at the KLaBMM at GIGCAS. Details of the analytical procedures may be found in Supplemental material DR1, analytical methods[1].

[1]GSA Data Repository item 2020035, analytical methods, Figs. DR1–DR3, and Tables DR1–DR5, is available at http://www.geosociety.org/datarepository/2020 or by request to editing@geosociety.org.

MAJOR AND TRACE ELEMENTS

Eclogite and Amphibolite Samples

Major and trace element compositions of the eclogite and amphibolite samples from the Gubaoquan area are given in Table 1. The eclogite and amphibolite samples show variable major element compositions that cluster in two groups. Group I samples are characterized by low SiO_2 (46.0–49.8 wt%) and Al_2O_3 (13.0–14.0 wt%), but relatively high MgO (6.84–8.44 wt%), CaO (7.58–11.1 wt%), and TiO_2 contents (1.07–2.12 wt%). In comparison with Group I, the samples from Group II have relatively high SiO_2 (59.2–60.6 wt%) and Al_2O_3 (14.4–17.9 wt%) but lower MgO (2.47–3.64 wt%), CaO (2.70–6.27 wt%), and TiO_2 contents (0.90–1.39 wt%; Table 1). Although variable in total alkali ($K_2O + Na_2O$ = 1.94–4.36 wt%), all the eclogite and amphibolite samples are relatively Na-enriched (K_2O/Na_2O ratios mostly <0.5; Table 1) and exhibit subalkaline-tholeiitic characteristics (Fig. 4A). In the immobile element based Zr/Ti versus Nb/Y classification diagram, Group I and Group II samples plot in the basalt and andesite fields, respectively (Fig. 4B), which is consistent with the classification in the total alkali versus silica (TAS) diagram (Fig. 4A).

The metabasalts contain higher Sc, V, Cr, Co, and Ni contents than meta-andesite. However, except for one meta-andesite, all the other samples have intermediate Ti/V ratios (22.5–39.0), which is similar to MORB and back-arc basin basalts (Shervais, 1982) (Fig. 4C). Metabasalts have V/Sc ratios between 6.95 and 9.77, which is significantly higher than in MORB (V/Sc = 6.7, Lee et al., 2005) and implies a relatively high oxygen fugacity condition. The metabasalts exhibit variable REE distribution patterns (Fig. 4D), from light rare earth element (LREE)-depleted ($(La/Yb)_N = 0.54$) to LREE-enriched ($(La/Yb)_N$ = 1.07–1.92), with negligible Eu anomalies (Eu/Eu* = 0.90–1.13). Although the metabasalts have MORB-like REE patterns (Fig. 4D), their Zr/Nb (mostly <4.5) and Zr/Sm (8–23) ratios are remarkably lower compared to N-MORB (Zr/Nb = 32; Zr/Sm = 28). The meta-andesite samples exhibit distinct REE patterns: the amphibolite sample is characterized by LREE-enriched ($(La/Yb)_N = 9.44$) pattern with pronounced Eu anomaly (Eu/Eu* = 0.70) while the eclogite sample has high rare earth element (HREE) pattern similar to that of the amphibolite but shows a significant fractionation between LREE and HREE (Fig. 4F). Although different in LREE enrichment, both the metabasalts and meta-andesites generally show unfractionated HREEs, as indicated by their $(Gd/Yb)_N$ ratios (1.18–1.28). Except for the

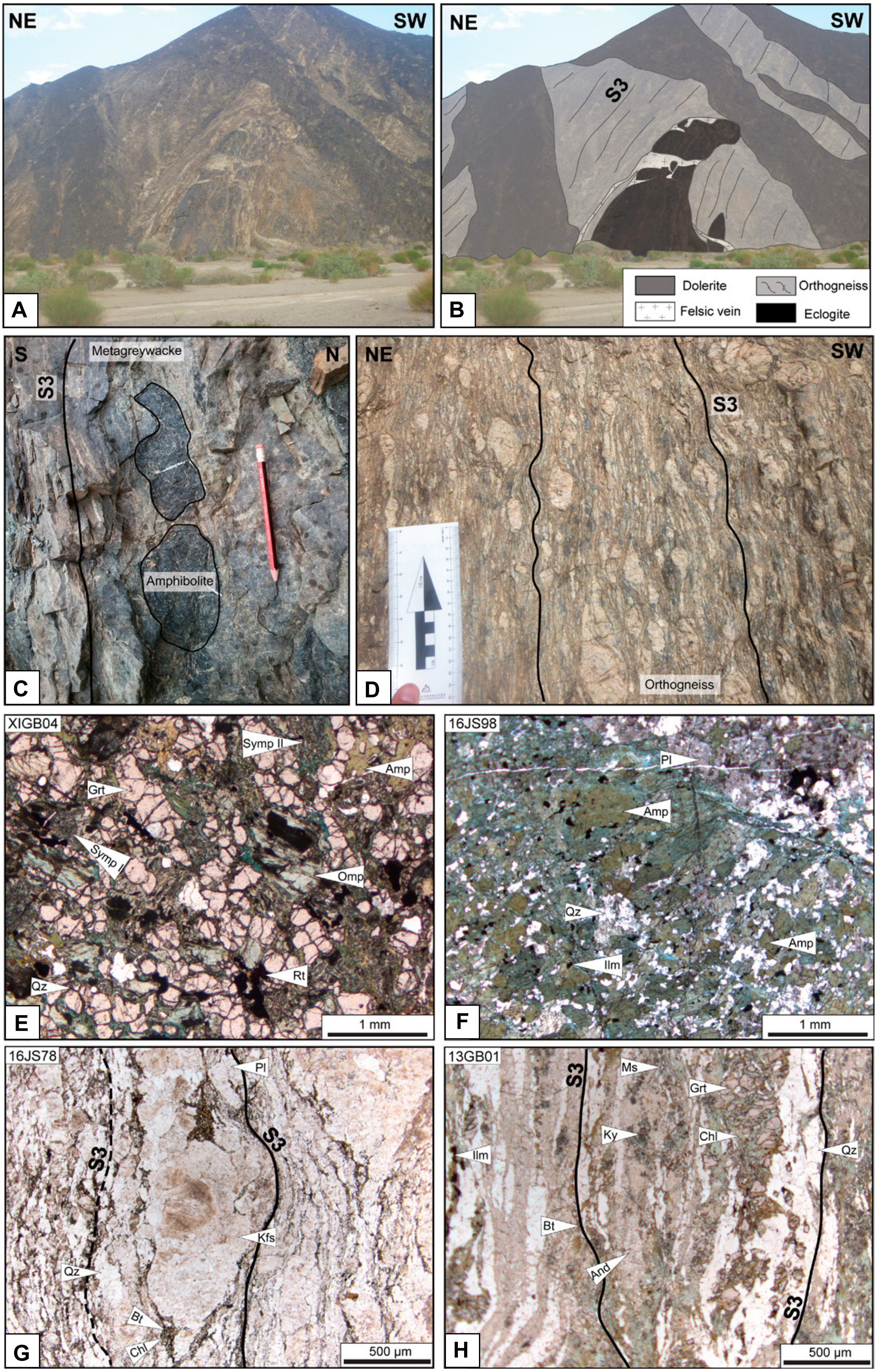

Figure 3. Field photographs of the tectono-structural features and thin section microphotographs of the Beishan Orogen (NW China) eclogite, amphibolite, orthogneiss, and metasediments. (A, B) Field relationships of eclogite, orthogneiss, and Permian doleritic dykes cross-cutting the main S3 fabric. (C) Amphibolite boudins occurring parallel to the S3 in metasediments. (D) Subvertical S3 fabric in orthogneiss. (E) Massive and isotropic texture in eclogite (sample XIGB04). (F) Massive and isotropic texture in amphibolite (sample 16JS98). (G) K-feldspar augen in the S3 fabric in orthogneiss (sample 16JS78). (H) Subvertical S3 fabric defined by alternation of biotite, muscovite, kyanite, and aluminosilicate-rich layers with quartz ribbons in metasediment (sample 13GB01). Chlorite and biotite in pressure shadows around garnet. Amp—amphibolite; And—andalusite; Bt—biotite; Chl—chlorite; Grt—garnet; Ilm—ilmenite; Kfs—K-feldspar; Ky—kyanite; Ms—muscovite; Omp—omphacite; Pl—plagioclase; Qz—quartz; Rt—rutile; Symp I—symplectite I; Symp II—sympletite II.

TABLE 1. MAJOR ELEMENT, TRACE ELEMENT, AND RARE EARTH ELEMENT COMPOSITIONS OF THE GUBAOQUAN ECLOGITE AND AMPHIBOLITE

Sample	16JS59	16JS79-1	16JS79-2	16JS79-4	16JS84	16JS98	XIGB04
Rock type	Amphibolite	Eclogite	Eclogite	Eclogite	Eclogite	Amphibolite	Eclogite
Location	40°59′20.1″ N 95°02′20.2″ E	40°59′15.5″ N 95°02′25.1″ E	40°59′15.5″ N 95°02′25.1″ E	40°59′15.5″ N 95°02′25.1″ E	40°59′15.5″ N 95°02′25.1″ E	40°59′22.0″ N 95°02′34.1″ E	40°59′15.5″ N 95°02′25.1″ E
Position	Small body	Main body	Main body	Main body	Main body	Small body	Main body
	Meta-basalt					Meta-andesite	
Major element (wt%)							
SiO_2	49.8	46.1	49.0	46.0	47.6	60.6	59.2
Al_2O_3	14.0	13.3	14.2	13.0	13.6	14.4	17.9
TiO_2	1.07	1.62	1.64	2.12	1.99	0.90	1.39
Fe_2O_{3T}	13.8	17.7	16.9	19.1	17.8	8.4	11.4
MnO	0.24	0.27	0.23	0.30	0.25	0.15	0.19
MgO	8.44	7.39	6.84	6.85	6.78	3.64	2.47
CaO	9.18	11.1	7.58	9.62	8.70	6.27	2.70
Na_2O	1.13	1.89	2.02	1.77	2.02	2.55	3.88
K_2O	1.06	0.14	0.56	0.17	0.26	1.28	0.48
P_2O_5	0.10	0.10	0.12	0.16	0.18	0.18	0.02
LOI*	1.03	0.04	0.54	1.30	0.53	0.88	0.52
Total	99.9	99.7	99.7	100.4	99.7	99.3	100.1
K_2O/Na_2O	0.94	0.07	0.28	0.10	0.13	0.50	0.12
Trace element and rare earth element (ppm)							
Li	8.77	12.3	7.46	7.95	4.58	7.50	6.05
Be	3.41	0.82	1.44	1.20	0.49	3.03	0.48
Sc	41.0	39.4	45.0	48.4	44.7	18.4	25.5
V	285	372	413	472	410	138	110
Cr	128	172	165	79.8	79.8	67.0	132.5
Co	48.8	57.8	47.9	65.6	69.1	23.1	20.0
Ni	68.3	64.9	54.7	47.9	86.4	24.5	22.7
Cu	63.1	103	83.5	155	270	49.0	17.5
Zn	85.2	126	138	142	148	92.6	65.1
Ga	15.6	15.9	16.9	17.0	16.9	17.0	10.6
Ge	1.18	1.38	1.42	1.58	1.46	1.51	2.49
As	2.15	1.00	1.58	4.87	0.88	1.47	1.21
Rb	45.3	5.13	30.4	7.37	12.9	60.8	13.6
Sr	107	130	107	105	120	200	513
Y	22.9	17.3	30.0	18.4	22.9	37.9	43.8
Zr	55.1	23.6	30.2	18.3	29.2	212	274
Nb	4.22	5.34	7.40	6.74	9.78	11.41	27.3
Cs	1.05	0.17	0.53	0.27	0.30	2.45	0.57
Ba	112	20.2	77.5	23.1	29.8	222	70.3
La	3.83	2.01	5.52	1.13	5.47	46.6	9.40
Ce	10.4	6.17	15.3	4.03	15.3	92.2	19.4
Pr	1.58	0.98	2.21	0.81	2.32	10.9	2.16
Nd	7.70	5.08	10.5	4.78	10.5	38.5	8.74
Sm	2.38	2.05	3.31	2.30	3.09	6.89	2.36
Eu	0.78	0.84	1.10	0.90	1.02	1.41	0.80
Gd	2.84	2.57	4.28	2.80	2.76	5.47	5.62
Tb	0.54	0.44	0.67	0.46	0.53	0.95	1.08
Dy	3.54	2.86	4.52	2.91	3.61	5.77	7.25
Ho	0.77	0.58	0.97	0.61	0.76	1.30	1.60
Er	2.05	1.47	2.71	1.72	2.11	3.61	4.24
Tm	0.29	0.20	0.35	0.22	0.30	0.51	0.59
Yb	1.87	1.34	2.41	1.51	2.04	3.54	3.95
Lu	0.28	0.23	0.36	0.23	0.31	0.56	0.63
Hf	1.43	0.65	0.93	0.70	0.91	5.18	6.75
Ta	0.28	0.32	0.38	0.34	0.55	0.56	2.08
W	0.36	0.13	0.21	0.32	0.18	0.53	1.90
Pb	5.72	1.97	1.03	2.61	1.48	18.8	3.50
Th	0.45	0.07	0.07	0.03	0.08	15.6	3.36
U	0.24	0.10	0.09	0.09	0.14	0.97	0.96
$(La/Yb)_N$	1.47	1.07	1.64	0.54	1.92	9.44	1.71
$(Gd/Yb)_N$	1.25	1.59	1.47	1.53	1.12	1.28	1.18
$(Nb/La)_{PM}$	1.06	2.57	1.29	5.75	1.72	0.24	2.80
Eu/Eu*†	0.92	1.13	0.90	1.09	1.07	0.70	0.67
Zr/Hf	38.5	36.5	32.5	26.1	32.0	40.9	40.6
Nb/Ta	14.9	16.9	19.4	19.7	17.8	20.5	13.1
Zr/Nb	13.1	4.42	4.08	2.72	2.99	18.6	10.0
Zr/Sm	23.2	11.5	9.11	7.96	9.47	30.8	116
V/Sc	6.95	9.45	9.17	9.77	9.18	7.52	4.32

*LOI—loss on ignition.

†Eu/Eu* = $2Eu_N/\sqrt{(SmN + GdN)}$; chondrite normalized values from Sun and McDonough (1989).

amphibolite sample of metandesitic composition, all the other samples do not exhibit pronounced negative Nb anomaly as evidenced by their relatively high $(Nb/La)_{PM}$ ratios (1.06–5.75; Table 1). In addition, the metabasalts have Zr/Hf ratios (mostly <39) lower, and Nb/Ta (mostly >17) ratios higher than N-MORB. In contrast, meta-andesites generally exhibit superchondritic Zr/Hf (~41) and variable Nb/Ta (13–20) ratios. In the primitive mantle normalized trace element diagram, the Group I samples show enrichment of large ion lithosphere elements (LILEs, e.g., Cs, Rb, Ba) relative to high field strength elements (HFSEs), and are characterized by Th, Zr, and Hf troughs as well as Pb spikes (Fig. 4E), as have been observed in some continent- or arc-derived eclogites (e.g., Tang et al., 2007; Utsunomiya et al., 2011). In contrast to the metabasalts, the two meta-andesite samples exhibit positive Zr-Hf and negative Ti anomalies, and almost identical HREEs (Fig. 4G). However, the two meta-andesites show distinct Nb(Ta)/LREE ratios. The eclogite sample with low LREE has super-chondritic Nb/La ratio and positive Nb-Ta anomaly, while the amphibolite sample with high LREE has relatively low Nb/La ratio and shows trough of Nb-Ta (Fig. 4G).

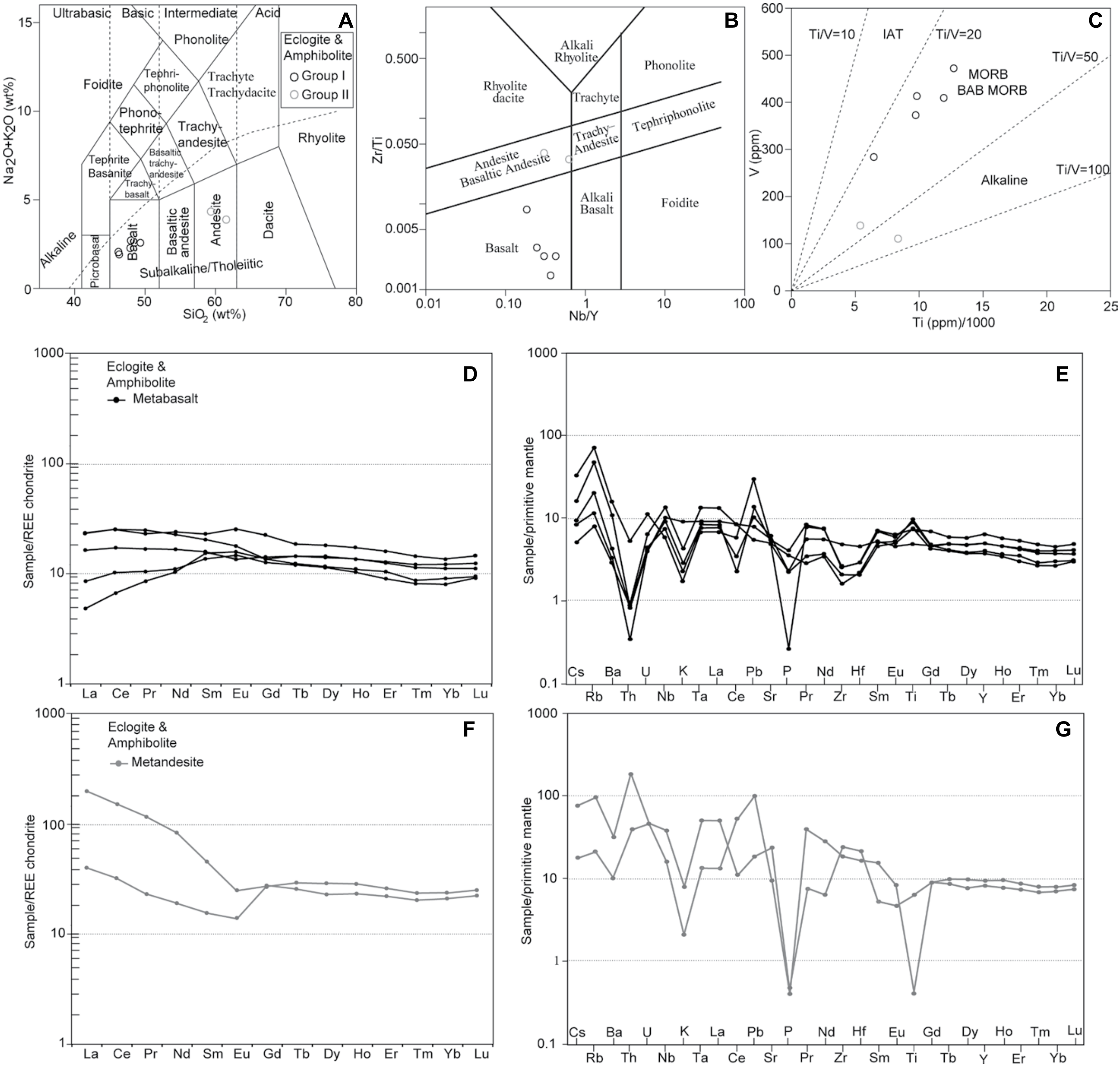

Figure 4. Geochemical discrimination diagrams for eclogite and amphibolite of the Beishan Orogen (NW China): (A) Total alkali-silica diagram of Le Bas et al. (1986). (B) Nb/Y versus Zr/Ti diagram of Pearce (1996). (C) The Ti/1000-V discrimination diagram of Shervais (1982). (D) Chondrite-normalized rare earth element (REE) patterns and (E) primitive mantle-normalized trace elements patterns of metabasalts. (F) Chondrite-normalized REE patterns and (G) primitive mantle-normalized trace elements patterns of meta-andesites. Chondrite and primitive mantle-normalizing values from Sun and McDonough (1989). IAT—island-arc tholeiites; BAB MORB—back-arc basalt mid-ocean ridge basalt.

Metasediments and Orthogneiss

Major and trace elements of orthogneiss and metasediments are given in Table 2. It is not always possible to distinguish in the field just on the macroscopic appearance of the rocks whether the gneiss is of igneous or sedimentary origin. The samples show a wide range of SiO_2 (50.9–71.4 wt%), Fe_2O_{3T} (3.25–13.3 wt%), MgO (0.73–4.81 wt%), Al_2O_3 (12.9–19.6 wt%), and CaO (1.24–5.19 wt%) contents and variable K_2O/Na_2O ratios (0.27–5.69). The calculated DF values (igneous and sedimentary parentage discriminatory analysis; DF = 10.44–0.21 SiO_2 – 0.32 Fe_2O_{3T} – 0.98 MgO + 0.55 CaO + 1.46 Na_2O + 0.54 K_2O; after Shaw, 1972) are negative (from –0.47 to –5.60) for almost all samples, confirming their sedimentary origin. Only

TABLE 2. MAJOR ELEMENT, TRACE ELEMENT, AND RARE EARTH ELEMENT COMPOSITIONS OF THE GUBAOQUAN METASEDIMENTS AND ORTHOGNEISS

Rock	Metasediment											Orthogneiss	
	Group I		Group II					Group III					
Sample	13GB01	13GB10	13GB02	13GB05	13GB06	13GB09	16JS92	16JS65	16JS67	16JS69	16JS70	16JS78	13GBA1
Location	40°59′ 21.2″ N, 95°02′ 19.4″ E	40°59′ 14.2″ N, 95°02′ 20.9″ E	40°59′ 21.2″ N, 95°02′ 19.4″ E	40°59′ 21.5″ N, 95°02′ 17.6″ E	40°59′ 21.5″ N, 95°02′ 17.6″ E	40°59′ 14.2″ N, 95°02′ 20.9″ E	40°59′ 16.2″ N, 95°02′ 44.8″ E	40°59′ 17.6″ N, 95°02′ 39.5″ E	40°59′ 18.9″ N, 95°02′ 39.6″ E	40°59′ 20.6″ N, 95°02′ 32.6″ E	40°59′ 20.6″ N, 95°02′ 32.6″ E	40°59′ 24.2″ N, 95°02′ 35.6″ E	40°59′ 24.4″ N, 95°02′ 29.4″ E
Major element (wt%)													
SiO_2	52.2	50.9	63.5	66.0	69.9	68.0	69.8	59.4	62.8	65.6	63.6	70.7	71.4
TiO_2	1.42	1.23	1.31	0.60	0.50	0.68	0.60	0.67	0.93	0.67	0.84	0.50	0.51
Al_2O_3	19.6	19.6	13.8	12.9	13.5	13.3	14.0	14.7	14.9	14.0	14.4	13.2	13.3
Fe_2O_{3T}	11.7	13.1	9.14	6.40	4.73	5.45	5.00	10.9	8.41	7.58	8.74	3.42	3.25
MnO	0.26	0.41	0.15	0.12	0.16	0.10	0.14	0.21	0.14	0.18	0.20	0.07	0.05
MgO	4.76	4.81	3.64	3.99	2.49	3.16	1.34	4.54	2.99	2.40	2.86	0.73	0.87
CaO	1.43	1.26	2.66	2.34	2.42	2.08	2.99	4.72	5.19	3.94	4.66	1.41	1.24
Na_2O	0.81	0.65	2.23	1.79	2.84	1.83	2.82	2.19	2.85	2.71	2.81	2.17	2.82
K_2O	3.41	3.70	0.76	2.95	2.29	3.01	1.67	1.87	0.78	1.14	0.82	5.98	4.93
P_2O_5	0.05	0.03	0.04	0.13	0.12	0.09	0.03	0.03	0.07	0.02	0.03	0.09	0.10
LOI*	3.87	3.44	2.20	2.27	0.62	1.69	0.99	0.91	0.83	0.96	0.74	0.90	1.19
Total	99.5	99.2	99.4	99.5	99.6	99.5	99.4	100.1	99.9	99.2	99.7	99.1	99.7
K_2O/Na_2O	4.20	5.69	0.34	1.65	0.81	1.64	0.59	0.85	0.27	0.42	0.29	2.76	1.75
DF§	–5.11	–5.60	–4.26	–3.88	–1.48	–3.24	–0.47	–3.15	–0.93	–1.38	–1.41	0.96	1.01
ICV#	1.21	1.29	1.43	1.40	1.14	1.22	1.04	1.70	1.43	1.33	1.45	N.A.†	N.A.†
CIA**	78	78	71	65	64	66	65	63	63	64	64	N.A.†	N.A.†
A/NK††	N.A.†	N.A.†	N.A.†	N.A.†	N.A.†	N.A.†	N.A.†	N.A.†	N.A.†	N.A.†	N.A.†	1.31	1.33
A/CNK§§	N.A.†	N.A.†	N.A.†	N.A.†	N.A.†	N.A.†	N.A.†	N.A.†	N.A.†	N.A.†	N.A.†	1.05	1.09
Trace element and rare earth element (ppm)													
Sc	30.5	36.7	24.5	12.4	10.3	10.8	9.08	24.8	20.5	20.6	21.6	5.44	6.57
Cr	122	129	136	40.0	40.5	57.4	90.9	145	74.5	118	83.4	18.7	12.2
Co	33.1	35.5	19.7	15.2	10.6	11.5	11.6	30.0	22.5	20.4	19.6	5.29	5.07
Ni	39.7	40.6	33.6	20.6	12.0	17.8	19.1	74.4	27.0	29.5	23.1	2.24	2.81
Cu	24.0	36.6	33.7	26.4	65.2	5.05	54.6	68.6	82.2	84.0	78.9	7.44	5.08
Rb	85.0	108	28.1	150	110	165	55.8	50.4	18.1	28.9	20.9	202	131
Sr	80.2	61.7	144	107	149	126	135	123	152	167	152	72.2	77.0
Y	58.5	84.3	51.5	25.9	26.4	26.0	30.7	25.7	13.7	28.8	19.7	36.2	43.1
Zr	268	294	287	165	173	270	264	156	183	263	205	236	218
Nb	18.0	15.4	14.2	11.2	11.3	11.2	10.5	5.27	9.70	7.95	9.55	11.0	11.2
Cs	1.59	2.43	0.55	4.86	3.73	4.27	1.91	3.21	0.77	0.86	0.85	3.37	0.90
Ba	1097	1054	198	417	453	421	239	661	225	358	257	525	461
La	57.0	49.3	24.4	31.6	32.1	28.6	31.6	6.68	15.6	18.9	19.0	43.9	61.5
Ce	106	90.3	43.7	65.0	66.9	61.6	61.1	11.2	28.8	40.3	34.5	83.6	117
Pr	13.1	10.6	4.72	7.92	7.91	7.26	7.30	1.19	3.16	3.76	3.72	9.27	14.3
Nd	47.8	39.1	17.6	29.2	29.4	26.9	25.4	4.76	11.0	14.0	13.0	32.8	49.1
Sm	8.84	8.28	5.21	6.01	5.83	4.81	4.66	1.53	2.05	2.42	2.34	6.34	9.14
Eu	2.04	1.87	1.17	1.25	0.94	1.07	1.13	1.06	1.10	1.21	1.18	1.01	0.94
Gd	9.25	10.5	7.58	5.12	4.97	4.41	3.77	2.17	1.95	2.59	2.24	6.27	8.10
Tb	1.56	1.97	1.33	0.80	0.78	0.69	0.72	0.44	0.29	0.46	0.35	0.94	1.23
Dy	9.31	13.5	8.59	4.38	4.53	4.12	4.57	3.41	1.91	3.63	2.67	5.75	7.30
Ho	2.03	2.98	1.73	0.87	0.89	0.87	1.03	0.85	0.47	0.98	0.65	1.23	1.52
Er	5.72	8.04	4.50	2.32	2.49	2.64	3.01	2.43	1.49	3.20	2.21	3.28	4.08
Tm	0.82	1.17	0.58	0.31	0.34	0.37	0.44	0.36	0.25	0.52	0.34	0.46	0.56
Yb	6.00	8.10	3.88	2.10	2.30	2.77	3.18	2.84	1.78	3.79	2.72	2.91	3.81
Lu	0.91	1.20	0.56	0.30	0.39	0.42	0.48	0.40	0.29	0.65	0.46	0.44	0.55
Hf	6.41	7.09	7.21	4.27	4.73	6.76	6.39	3.86	4.32	6.55	4.55	6.25	6.50
Ta	0.71	0.61	0.68	0.65	0.71	0.79	0.58	0.22	0.54	0.39	0.46	0.81	0.97
Pb	4.82	3.27	13.9	29.3	46.4	19.5	23.9	11.2	8.46	10.1	9.54	27.1	29.6
Th	14.3	7.77	2.70	13.8	16.6	11.4	4.75	0.37	0.90	5.02	0.92	35.6	49.7
U	0.87	0.78	0.57	2.17	2.50	1.66	0.54	0.25	0.31	0.60	0.37	3.23	4.45
ΣREE	285	255	129	173	179	160	154	39.8	71.6	102	86.6	237	334
$(La/Yb)_N$	6.81	4.37	4.50	10.79	9.98	7.41	7.12	1.69	6.28	3.59	5.02	10.8	11.6
$(Dy/Yb)_N$	1.04	1.12	1.48	1.40	1.31	0.99	0.96	0.81	0.72	0.64	0.66	1.28	1.32
K/Rb	333	286	224	163	173	151	248	308	358	328	326	246	313
Eu/Eu***	0.69	0.62	0.57	0.69	0.53	0.71	0.82	1.77	1.68	1.48	1.58	0.49	0.34

*LOI—loss on ignition.
†N.A.—not applicable.
§DF—10.44–0.21SiO_2 – 0.32Fe_2O_3T – 0.98MgO + 0.55 CaO + 1.46Na_2O + 0.54K_2O; after Shaw (1972).
#ICV—(Fe_2O_3 + K_2O + Na_2O + CaO + MgO + TiO_2)/Al_2O_3.
**CIA—Al_2O_3/(Al_2O_3 + CaO + Na_2O + K_2O) × 100.
††A/NK—Al_2O_3/(Na_2O + K_2O).
§§A/CNK—molar Al_2O_3/(CaO + Na_2O + K_2O).
***Eu/Eu*—2 × Eu_N/(Sm_N + Gd_N); chondrite normalized values from Sun and McDonough (1989).

samples 16JS78 and 13GBA1 have positive DF values (0.96 and 1.01), consistent with their igneous origin (Table 2).

The metasediment samples display a wide range of major element contents. Aluminosilicate-bearing metasediments have Al-rich composition (Al_2O_3 = 19.6 wt%) compared to Al-poor metasediments (Al_2O_3 = 12.9–14.9 wt%). Al-poor metasediments are characterized by high SiO_2 (59.3–69.9 wt%), Na_2O (1.78–2.85 wt%), and CaO (2.08–5.19 wt%) contents. Al-rich metasediments are characterized by low SiO_2 (50.9–52.2 wt%), Na_2O (0.65–0.81 wt%), and CaO (1.26–1.43 wt%) contents. All samples have low chemical index of alteration [CIA = Al_2O_3/(Al_2O_3 + CaO + Na_2O + K_2O) × 100, molar ratio] and high index of compositional variability [ICV = (Fe_2O_3 + K_2O + Na_2O + CaO + MgO + TiO_2)/Al_2O_3, molar ratio], suggesting an immature source affected by weak chemical weathering (Fig. 5A; Cox et al., 1995; Nesbitt and Young, 1982). In the log(Na_2O/K_2O) versus log(SiO_2/Al_2O_3), most samples are classified as greywackes with minor litharenite (Fig. 5B; Pettijohn et al., 1987).

In the TAS diagram, the orthogneiss plots in the granite field, suggesting a granitic protolith

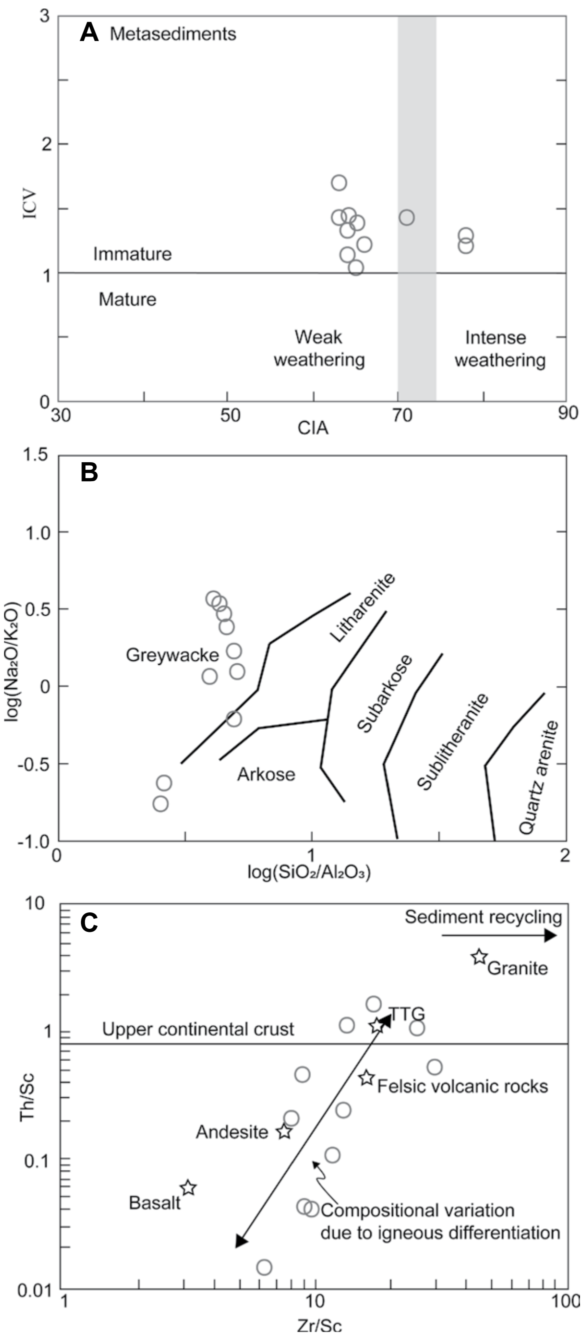

Figure 5. Geochemical characterization diagrams for the Gubaoquan metasediments, NW China: (A) CIA-ICV classification diagrams of Nesbitt and Young (1984) and Cox et al. (1995). (B) Classification diagram after Pettijohn et al. (1987). (C) Zr/Sc versus Th/Sc diagram after McLennan et al. (1993). CIA—$Al_2O_3/(Al_2O_3 + CaO + Na_2O + K_2O) \times 100$; ICV—$(Fe_2O_3 + K_2O + Na_2O + CaO + MgO + TiO_2)/Al_2O_3$; TTG—tonalite-trondhjemite-granodiorite.

(Fig. 6A). The orthogneiss samples are high-K calc-alkaline and peraluminous, with A/CNK index of 1.31 and 1.33 (Figs. 6B and 6C; Table 2).

The metasediments have rather wide composition ranges in REEs and LILEs (Table 2). Because Th and Sc are enriched in silicic and basic rocks, and do not vary much during sedimentary recycling, Th/Sc ratio is commonly used to trace the provenance of sediments, while Zr/Sc ratio generally reflects the degree of sediment recycling with zircon enrichment and can be considered as a possible indicator of heavy mineral concentration (McLennan et al., 1993; Cullers, 1994). In the Th/Sc versus Zr/Sc diagram, plots of the metasediments form a positive trend, suggesting that the geochemical variations of the metasediments probably reflect a variable proportion of contribution from mafic and felsic sources (Cullers, 1994; Fig. 5C). Three groups of metasediments can be distinguished based on their chondrite- and primitive mantle-normalized REE and trace element distribution patterns. Group A samples are characterized by enriched LREEs ($(La/Yb)_N = 4.37–6.81$), flat HREE profile ($(Dy/Yb)_N = 1.04–1.12$), and high REE concentrations ($\Sigma REE = 255–285$; Fig. 7A; Table 2). Group B samples are also characterized by enriched LREEs ($(La/Yb)_N = 4.51–10.80$) and rather flat HREE ($(Dy/Yb)_N = 0.96–1.48$), but they have low REE concentrations ($\Sigma REE = 129–179$; Fig. 7C; Table 2). Both the Group A and Group B samples have negative Eu anomalies ($Eu/Eu^* = 0.53–0.83$; Figs. 7A and 7C). In the primitive mantle normalized diagrams, the Group A and Group B samples have trace element patterns characterized by depletion in HFSEs (Nb, Ta, and Ti), by strong negative Sr and negative P anomalies and positive Th and Pb anomalies, which are features characteristic to the average composition of the middle crust (Rudnick and Gao, 2003; Figs. 7B and 7D). Group C samples are also enriched in LREEs ($(La/Yb)_N = 1.69–6.29$) and have incompatible element patterns similar to those of the middle and upper continental crust (Fig. 7E) (Rudnick and Gao, 2003). A distinctive feature of the Group C samples is the relative enrichment of HREE over MREEs (middle rare earth elements) ($(Dy/Yb)_N = 0.64–0.81$) as well as positive Eu anomalies ($Eu/Eu^* = 1.48–1.77$) (Fig. 7F).

The orthogneiss samples are enriched in LREEs ($(La/Yb)_N = 10.8–11.6$) with rather flat HREE patterns ($(Dy/Yb)_N = 1.28–1.32$ (Fig. 7G; Table 2). They display negative Eu anomalies ($Eu/Eu^* = 0.34$ and 0.49; Table 2), indicating fractionation of plagioclase from the melts and/or inheritance from the source material. In the primitive mantle-normalized diagrams, orthogneisses are characterized by depletion in HFSEs (Nb, Ta, and Ti) with strong negative Sr and P anomalies and positive Th and Pb anomalies (Fig. 7H), which is a similar feature as in the metasediments.

ZIRCON GEOCHRONOLOGY, HF ISOTOPE COMPOSITIONS AND TRACE ELEMENT CHEMISTRY

Eclogite 17JS102

Zircon from eclogite 17JS102 is subhedral with sizes ranging from 40 to 150 μm. CL images reveal that zircon has either core-rim structures or is sub-rounded with homogeneous internal texture (Fig. 8C). Dark zircon cores having CL-sector patterns with embayments are interpreted as xenocrystic cores affected by dissolution-precipitation. Zircon cores having weak oscillatory zoning are surrounded by CL-bright rims ranging from 10 to 80 μm in width and these are in places surrounded by even brighter and thinner rims (<10 μm). Sub-rounded grains are CL-bright with size less than 80 μm and are interpreted as metamorphic. Among thirty analyzed spots, twenty analyses of zircon cores yield $^{206}Pb/^{238}U$ ages ranging from 831 ± 6 Ma to 1023 ± 9 Ma. Four analyses of CL-dark cores interpreted

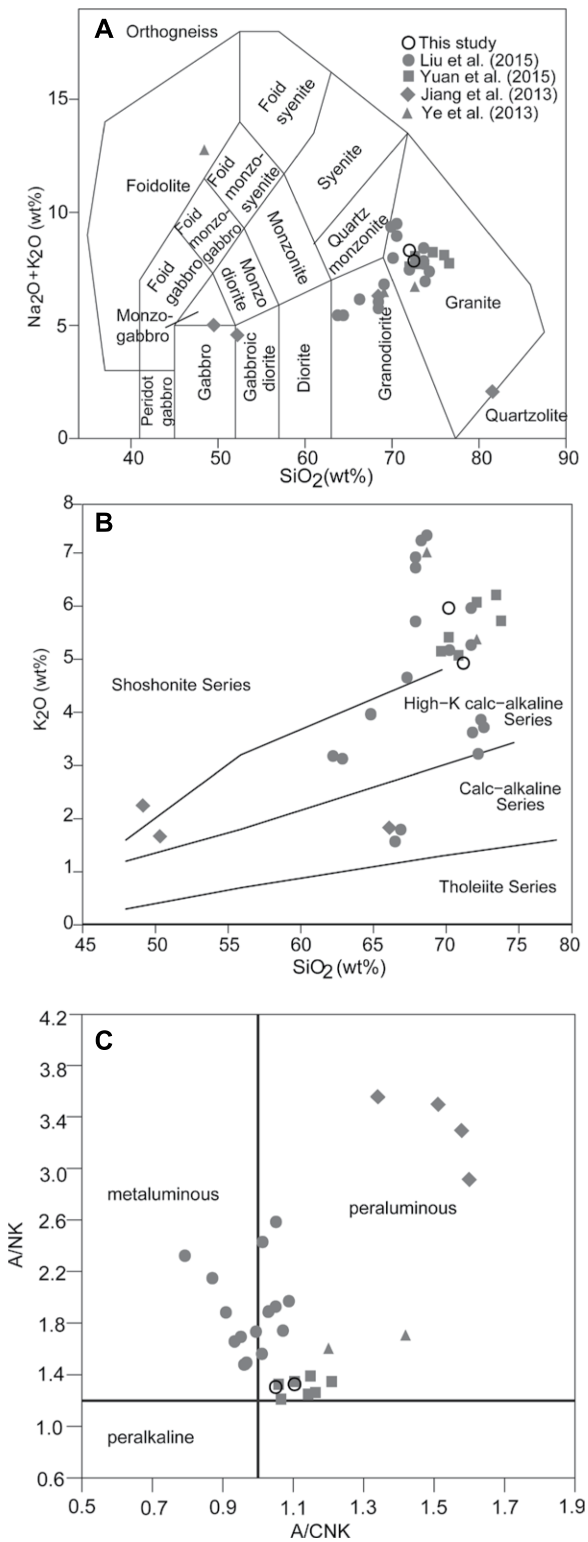

Figure 6. Geochemical discrimination diagrams for the Gubaoquan orthogneisses. (A) The total alkali versus silica discrimination diagram of Middlemost (1994). (B) SiO_2 versus K_2O diagrams of Frost et al. (2001). (C) A/NK (Al_2O_3/($Na_2O + K_2O$)) versus A/CNK (molar Al_2O_3/($CaO + Na_2O + K_2O$)) diagram of Maniar and Piccoli (1989). Available data points for the Beishan orthogneiss are from Liu et al. (2015), Yuan et al. (2015), Jiang et al. (2013), and Ye et al. (2013).

as xenocrysts with sector patterns yield oldest $^{206}Pb/^{238}U$ ages of 932 ± 7 Ma, 973 ± 9 Ma, 1009 ± 12 Ma, and 1023 ± 9 Ma. The analyses of eleven zircon cores with oscillatory zoning, interpreted as of magmatic origin, yield a weighted mean $^{206}Pb/^{238}U$ age of 889.3 ± 4.8 Ma (Fig. 8A; Table DR1 [footnote 1]). Among all the twenty analyzed zircon cores (xenocrystic and magmatic), fifteen spots display consistent elevated REE contents characterized by positive and steep HREE distribution as well as by deep negative Eu anomaly (Eu/Eu* = 0.09–0.24). One spot in a magmatic core has similar REE patterns and positive Eu anomaly (Eu/Eu* = 1.43). The remaining four analyzed spots in three magmatic cores and one xenocrystic core are characterized by elevated REEs and show flat or slightly depleted HREEs. The eight spots have deep negative Eu anomalies (0.04–0.43) (Fig. DR1; Table DR2 [footnote 1]). A total of ten analyzed zircon rims have $^{206}Pb/^{238}U$ ages ranging from 469 ± 6 Ma to 455 ± 4 Ma and yield a concordia $^{206}Pb/^{238}U$ age of 465.0 ± 3.8 Ma (Fig. 8B). All the analyzed spots in zircon rims have consistently elevated REE with flat HREE profiles and slightly negative to positive Eu anomaly (Eu/Eu* = 0.39–0.69) (Fig. DR1; Table DR2). The zircon cores have Th/U ratios (0.02–1.14) significantly higher than the rims (0.03–0.04), corresponding to magmatic and metamorphic origin, respectively (Table DR1).

Representative magmatic cores and metamorphic rims of zircon with high degree of concordance were chosen for in situ multicollector–inductively coupled plasma–mass spectrometry zircon Hf isotope analyses (Fig. 9; Table DR3 [footnote 1]). Fifteen analyses on zircon magmatic cores with ages between 831 Ma and 1022 Ma show relatively homogeneous $^{176}Hf/^{177}Hf$ ratios (0.282037–0.282306), corresponding to $\varepsilon_{Hf}(t)$ values from –5.01 to +2.30 and one-stage model ages (T_{DM}) of 1.59–2.08 Ga. In box-plot diagram, the median for $\varepsilon_{Hf}(t)$ values is –1.46 and the median for T_{DM} ages is 1.50 Ga (Fig. 9). Six analyses on zircon metamorphic cores or grains with ages ranging from 455 Ma to 467 Ma also show homogeneous $^{176}Hf/^{177}Hf$ ratios (0.282038–0.282178), equivalent to $\varepsilon_{Hf}(t)$ values from –10.76 to –15.74 and T_{DM} ages from 1.49 to 1.66 Ga (Fig. 9).

Amphibolite 16JS98

Zircon from amphibolite is euhedral to subhedral with size ranging from 80 to 220 µm. CL images reveal that zircon is characterized by core-rim structures (Fig. 8G). Zircon cores have oscillatory zoning characteristic of magmatic textures or present embayments interpreted as a result of dissolution-precipitation. Zircon cores are surrounded by dark and bright rims ranging from 10 to 40 µm, with the dark rims in places surrounding the bright rims. Among thirty-two analyzed spots, twelve analyses on magmatic zircon cores yield $^{206}Pb/^{238}U$ ages ranging from 1358 ± 10 Ma to 1836 ± 12 Ma. In this group, eight magmatic cores yield a weighted mean $^{206}Pb/^{238}U$ age of 1378 ± 15 Ma (Fig. 8D; Table DR1). Older magmatic cores with $^{206}Pb/^{238}U$ ages ranging from 1445 ± 11 Ma to 1836 ± 12 Ma are interpreted as inherited xenocrysts. Six spots on bright zircon cores and rims yield $^{206}Pb/^{238}U$ ages

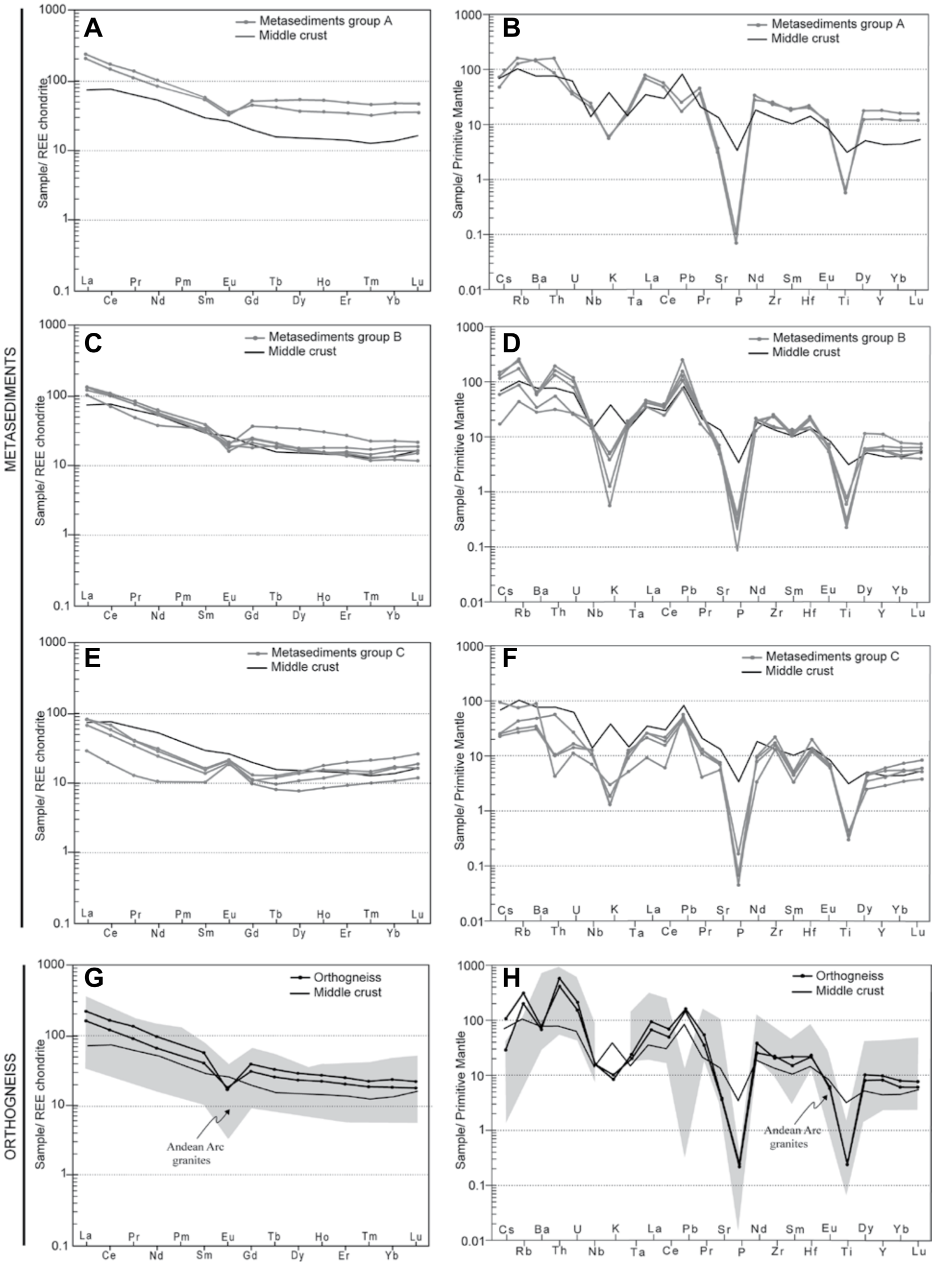

Figure 7. Chondrite-normalized rare earth element (REE) patterns and primitive mantle-normalized trace element patterns metasediments of Group A (A, B), Group B (C, D), and Group C (E, F) metasediment form the Beishan Orogen, NW China. (G) Chondrite-normalized REE patterns and (H) primitive mantle-normalized trace elements patterns of orthogneiss from the Beishan Orogen. Chondrite- and primitive mantle-normalizing values are from Sun and McDonough (1989). Data shown for Andean Arc granites are from the GEOROC database (http://georoc.mpch-mainz.gwdg.de/georoc/Start.asp).

ranging from 1247 ± 9 Ma to 1274 ± 17 Ma, which yield a weighted mean $^{206}Pb/^{238}U$ age of 1258 ± 10 Ma (Fig. 8E; Table DR1). Eight spots on dark zircon rims surrounding magmatic or xenocrystic cores yield $^{206}Pb/^{238}U$ ages ranging from 907 ± 12 Ma to 917 ± 13 Ma and a concordia $^{206}Pb/^{238}U$ age of 910.9 ± 3.0 Ma (Fig. 8F; Table DR1). Six other spots in CL-sector cores or in zircon rims yield $^{206}Pb/^{238}U$ ages ranging from 698 ± 13 Ma to 1337 ± 8 Ma (Fig. 8D). All the analyzed spots in zircon cores and rims have similar REE patterns with elevated REE contents, steep HREE slope and a negative Eu anomaly (Eu/Eu* = 0.02–0.22) (Fig. DR1; Table DR2). Bright and dark zircon rims have Th/U ratios ranging from 0.10 to 0.35 and from 0.08 to 0.92, respectively. Magmatic grains have Th/U ratios ranging from 0.09 to 0.60 (Table DR1).

Orthogneiss 16JS78

Zircon from orthogneiss 16JS78 is mostly stubby and subhedral and 80–220 μm in size, with prismatic aspect ratios of 1:3. CL images show that most zircon grains display oscillatory zoning (Fig. 10C). Nevertheless, several zircons have dark xenocrystic core with absence of zoning or with patchy zoning interpreted to be due to solid-state recrystallization (Hoskin and Black, 2000). Among sixteen analyzed spots, four spots in patchy or homogeneous zircon cores yield $^{206}Pb/^{238}U$ ages ranging from 1008 ± 18 Ma to 889 ± 9 Ma (Fig. 10A; Table DR1). Ten other spots in the oscillatory-zoned magmatic zircons yield a concordia $^{206}Pb/^{238}U$ age of 867.5 ± 1.9 Ma (Fig. 10B). Two spots in oscillatory-zoned zircon cores yield discordant $^{206}Pb/^{238}U$ ages of 785 ± 4 Ma and 825 ± 5 Ma, probably due to Pb-loss. Th/U ratios of all the zircon grains including xenocrystic cores range from 0.15 to 1.14 with an average Th/U ratio of 0.42, which confirms the magmatic origin of these zircons (Table DR1).

Metagreywacke 13GB01

Zircon from metagreywacke 13GB01 is mostly subhedral, sub-rounded to multifaceted, with prismatic aspect ratios of 1:1–2:1. The zircon varies in size from 60 to 130 μm. CL images show that the zircon mostly has homogeneously textured dark cores and cores characterized by sectoral zoning, both surrounded by thin and bright rims (Fig. 10G). Data from sixteen spots in the dark homogeneous or sectoral zircon cores yield $^{206}Pb/^{238}U$ ages ranging from 760 ± 21 Ma to 922 ± 8 Ma (Fig. 10D; Table DR1). Data from six spots on bright rims around dark cores yield a weighted mean $^{206}Pb/^{238}U$ age of 845.6 ± 6.9 Ma (Figs. 10E and 10F). The other three spots on bright rims give $^{206}Pb/^{238}U$ concordant ages of 870.7 ± 10.8 Ma, 798.1 ± 8.5 Ma, and 438.8 ± 5 Ma. The youngest age of ca. 760 Ma is interpreted as the maximum deposition age. Th/U ratio from zircon cores varies from 0.08 to 1.01 whereas zircon rims show lower Th/U ratios ranging from 0.02 to 0.74 (Table DR1).

Metagreywacke 16JS67

Zircon from the metagreywacke 16JS67 is 70–180 μm in size, dominated by subhedral, sub-rounded to multifaceted crystals with prismatic aspect ratios of 1:1–2:1 (Fig. 10I). CL images show that the analyzed zircon has mostly sectoral dark cores, although a few have homogeneous dark cores. Zircon cores are

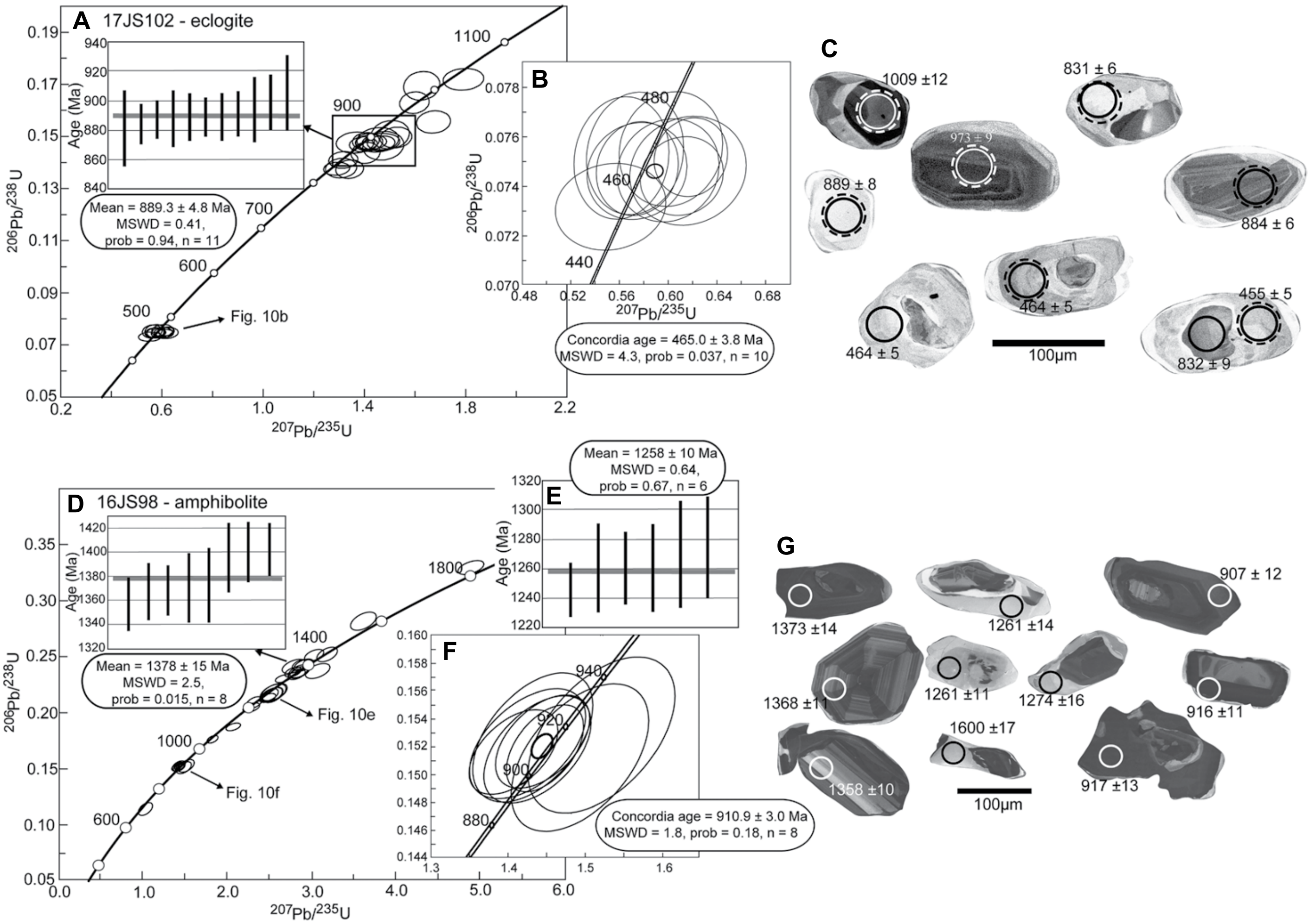

Figure 8. Concordia diagrams, ^{206}Pb/^{238}U weighted average age plots and representative cathodoluminescence images of magmatic and metamorphic zircon of the eclogite 17JS102 (A–C) and amphibolite 16JS98 (D–G). Error ellipses and error bars are 2σ in the concordia diagrams. Spots for age and for Hf isotopic composition analyzes are given by circles and dashed circles, respectively. MSWD—mean square weighted deviation; prob—probability; n—number of analysis.

surrounded by bright rims with width ranging from 10 to 50 µm (Fig. 10I). Data from eleven analyzed zircon cores yield ^{206}Pb/^{238}U ages ranging from 1318 ± 11 Ma to 841 ± 8 Ma, and eight analyzed spots in zircon rims yield ^{206}Pb/^{238}U ages ranging from to 1307 ± 13 Ma to 813 ± 6 Ma. All spots lie on a discordia, which gives an upper intercept age at 1461 ± 44 Ma and a lower intercept age at 750 ± 34 Ma (Fig. 10H). Zircon cores and rims display Th/U ratios ranging from 0.07 to 0.37 and from 0.05 to 0.92, consistent with a magmatic origin (Table DR1).

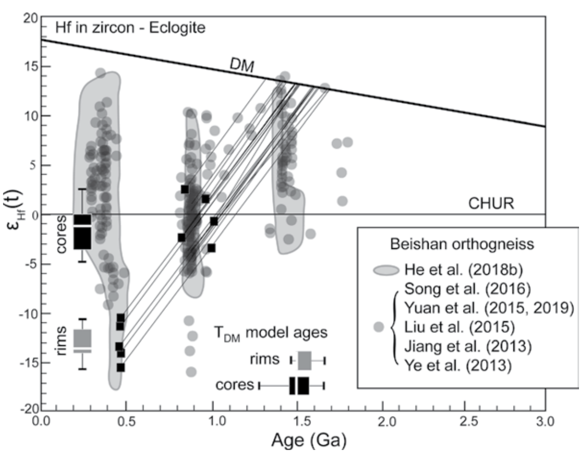

Figure 9. Diagram of ε_{Hf}(t) values versus age (Ma) for zircon cores and rims in eclogite 17JS102. The results are given in the form of box-plots. The line across the box represents the median value of the data and ranges are the interquartile ranges (differences between third and first quartile, Q3–Q1). Dots are analysis points beyond whiskers (outliers). The number of analyses are marked. Shown are the plots of the orthogneiss from the Beishan Orogen (Ye et al., 2013; Jiang et al., 2013; Liu et al., 2015; Yuan et al., 2015, 2019; Song et al., 2016; He et al., 2018b). CHUR—chondritic uniform reservoir; DM—depleted mantle.

ZIRCON AGES AND COMPOSITIONAL CHARACTERISTICS

Zircon U-Pb dating of magmatic cores in the eclogite 17JS102 yields crystallization age of the

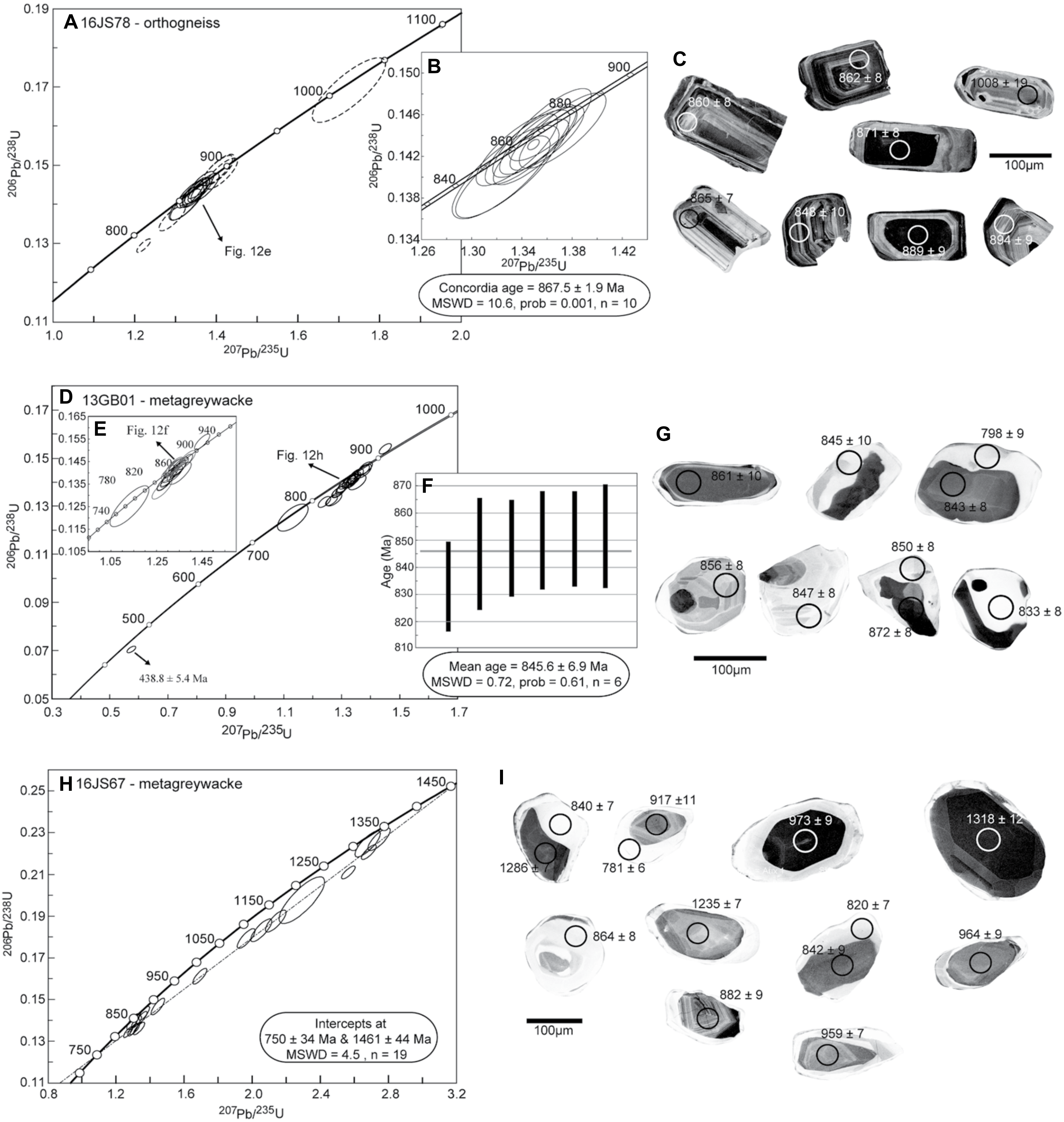

Figure 10. Concordia diagrams, $^{206}Pb/^{238}U$ weighted average age plots and representative cathodoluminescence images of zircon cores and rims in orthogneiss 16JS78 (A–C), metagreywacke 13GB01 (D–F), and metagreywacke 16JS67 (H, I). Error ellipses and error bars are 2σ in the concordia diagrams. MSWD—mean square weighted deviation; prob—probability; n—number of analysis.

protolith at 889.3 ± 4.8 Ma, whereas metamorphic rims yield a concordia age of 465.0 ± 3.8 Ma corresponding to Ordovician eclogite-facies metamorphism (Figs. 8A and 8B). Detailed interpretation of zircon compositional characteristics for eclogite 17JS102 is given in Supplemental material DR2. Zircon U-Pb dating of cores in amphibolite 16JS98 yield an age of 1378 ± 15 Ma (Fig. 8D). Because these zircon cores are the only grains characterized by magmatic oscillatory zoning apart from older inherited grains, we consider this age as corresponding to the crystallization of the andesitic protolith of the rock. This is particularly consistent with the crystallization ages of (1) amphibolite from the adjacent Chinese Central Tianshan (1384 ± 15 Ma; He et al. 2018a) and (2) granodiorites and granitic gneisses from the southern Beishan Orogen (1401–1450 Ma; He et al., 2015; Yuan et al., 2019). Altogether, this indicates the existence of a reworked Mesoproterozoic crust in the Beishan Orogen (He et al., 2018b; Yuan et al., 2019). Zircon U-Pb dating of rims from two different types of zircons from sample 16JS98 indicates that the protolith underwent two metamorphic events at ca. 1258 Ma and 911 Ma.

Zircon U-Pb dating of orthogneiss 16JS78 shows that the granitic protolith of the orthogneiss crystallized at 867.5 ± 1.9 Ma (Fig. 10A), consistent with previously published zircon U-Pb crystallization ages (871–905 Ma; Ye et al., 2013; Liu et al., 2015; Yuan et al., 2015). Zircon U-Pb dating of zircon cores from the metagreywacke 13GB01 shows crystallization ages ranging from 760 ± 21 to 922 ± 8 Ma. The magmatic Th/U ratio (Th/U > 0.03) of most zircon spots suggests that the obtained ages might correspond to the formation ages of their source rocks. Despite rather high Th/U ratios, bright zircon rims from sample 13GB01 indicate the existence of a metamorphic event at ca. 845.6 ± 6.9 Ma (Fig. 10). The upper intercept of 1461 ± 44 Ma calculated for the metagreywacke sample 16JS67 is interpreted as the age of an old crustal component involved in the formation of the granitic protolith of the metasediments (Fig. 10H). The lower intercept of 750 ± 34 Ma is interpreted as a Neoproterozoic crustal reworking event recorded in the Gubaoquan area.

In summary, zircon U-Pb ages from amphibolite and metagreywacke indicate presence of a Mesoproterozoic crust in the Beishan Orogen. Similar zircon U-Pb ages of eclogite and orthogneiss indicate the nearly coeval occurrence of mafic and felsic magmatism in the Neoproterozoic. The zircon rim U-Pb ages of the amphibolite indicate that this thermal event is preceded by a metamorphic event at ca. 911 Ma, whereas zircon rim U-Pb ages of the metagreywacke reflect a metamorphic event at ca. 846 Ma

WHOLE-ROCK SR-ND ISOTOPE COMPOSITIONS

Whole-rock Sr-Nd isotopic results for five eclogite and two amphibolite samples are listed in Table 3. The $\varepsilon_{Nd}(t)$ has been calculated on the basis of zircon U-Pb ages of 889 Ma (samples 16JS59, 16JS79-1, 16JS79-2, 16JS79-4, and 16JS84) and 1378 Ma (sample 16JS98). All samples are characterized by variable $^{147}Sm/^{144}Nd$ ratios (0.11–0.30) and $^{87}Sr/^{86}Sr_i$ ratios (0.7056–0.7149) (Fig. 11A), the samples have variably negative $\varepsilon_{Nd}(t)$ values and Meso- to Paleoproterozoic two-stage model ages (T_{DM2} = 1567–2391 Ma) (Fig. 11B; Table 3). Among the metabasite samples, the eclogite samples from the main eclogite body show a relatively limited range of $^{87}Sr/^{86}Sr_i$ ratios (0.7056–0.7104) and $\varepsilon_{Nd}(t)$ values (–4.3 to –10.3), whereas two amphibolite samples have remarkably high $^{87}Sr/^{86}Sr_i$ ratios (>0.714) and $\varepsilon_{Nd}(t)$ values of –0.2 to –3.7 (Fig. 11A).

MONAZITE GEOCHRONOLOGY AND TRACE ELEMENT CHEMISTRY

In metagreywackes, both Paleozoic and Meso- to Neoproterozoic monazite grains were found. In this study, only Meso- to Neoproterozoic monazite grains are chosen for geochronological and compositional investigations and Paleozoic metamorphic grains are not described here. Compositional maps for Meso- to Neoproterozoic monazite are presented in Figure DR2 (see footnote 1). Monazite geochronological characteristics and trace element distributions are presented in Figures 12 and 13, respectively.

Metagreywacke 13GB10

In metagreywacke 13GB10, two monazite grains, one in garnet and one in a matrix, were chosen for further structural, textural, and geochronological studies. The grain in the matrix is xenomorphic with irregular shape and notable fractures, and 120 µm in size. The grain enclosed in garnet is subhedral and 60 µm in size. The matrix monazite is U- and Th-poor and presents embayments in its core and flank, which tend to be poor in Y (Fig. DR2). The monazite grain in garnet contains biotite inclusion and is compositionally homogeneous, rich in U and poor in Th. Analyses on cores and rims of the two monazite grains yield $^{238}U/^{206}Pb$ ages ranging from 846 ± 13 Ma to 931 ± 15 Ma (Figs. 12A and 12B; Table DR4 [footnote 1]). All the spots show HREE-depleted patterns and two types of REE patterns of the analyzed spots can be recognized: type I spots with ages of 846 Ma, 860 Ma, and 931 Ma have higher HREE concentrations than the type II spots of 860 Ma and 900 Ma (Fig. 13A). All spots have negative Eu anomaly (Eu/Eu* = 0.08–0.51; Fig. 13; Table DR5 [footnote 1]).

Metagreywacke 13GB01

In metagreywacke 13GB01, three monazite grains in garnet and matrix were chosen for studies. The grains included in garnet are subhedral

TABLE 3. RB-SR AND SM-ND ISOTOPIC COMPOSITIONS OF THE GUBAOQUAN ECLOGITE AND AMPHIBOLITE

Sample	Rock type	Age (Ma)	Sr (ppm)	Rb (ppm)	Sm (ppm)	Nd (ppm)	$^{87}Sr/^{86}Sr$	$^{87}Sr/^{86}Sr$ (±2σ)	$(^{87}Sr/^{86}Sr)_i$	$^{147}Sm/^{144}N$	$^{143}Nd/^{144}Nd$ (±2σ)	$(^{143}Nd/^{144}Nd)_i$	$\varepsilon_{Nd}(t)$*	T_{DM2} (Ma)	ƒSm/Nd
16JS59	Amphibolite	889	107	45.3	2.38	7.70	1.18268069	0.733404 ± 7	0.71837944	0.19004866	0.512587 ± 9	0.511478827	–0.2	1567	–0.033815
16JS79-I	Eclogite	889	130	5.13	2.05	5.08	0.11057093	0.707000 ± 10	0.70559533	0.24812397	0.512599 ± 7	0.511152191	–6.6	2094	0.261434
16JS79-II	Eclogite	889	107	30.4	3.31	10.5	0.79541593	0.717244 ± 8	0.70713918	0.19475574	0.512335 ± 7	0.51119938	–5.7	2011	–0.009884
16JS79-IV	Eclogite	889	105	7.37	2.30	4.78	0.19558608	0.712915 ± 9	0.71043031	0.29585473	0.512690 ± 7	0.510964873	–10.3	2391	0.504091
16JS84	Eclogite	889	120	12.9	3.09	10.5	0.30025099	0.712614 ± 10	0.70879967	0.18060148	0.512325 ± 9	0.511271914	–4.3	1898	–0.081843
16JS98	Amphibolite	1378	200	60.8	6.89	38.5	0.84950743	0.731701 ± 9	0.71491448	0.11003658	0.511666 ± 7	0.510669855	–3.7	2258	–0.440587
XIGB04	Eclogite	889	513	13.6	2.36	8.74	0.07392987	0.708512 ± 10	0.70757281	0.16602716	0.512052 ± 7	0.511083897	–8.0	2200	–0.155937

*$\varepsilon_{Nd}(t)$—[$(^{143}Nd/^{144}Nd)_{sample}/(^{143}Nd/^{144}Nd)_{CHUR} - 1$] × 10000, $(^{143}Nd/^{144}Nd)_{CHUR}$ = 0.51263, $(^{147}Sm/^{144}Nd)_{CHUR}$ = 0.1967; λ = 6.54 × 10^{-6} $year^{-1}$; t—zircon crystallization time; CHUR—chondritic uniform reservoir; T_{DM2}—Two-stage model age.

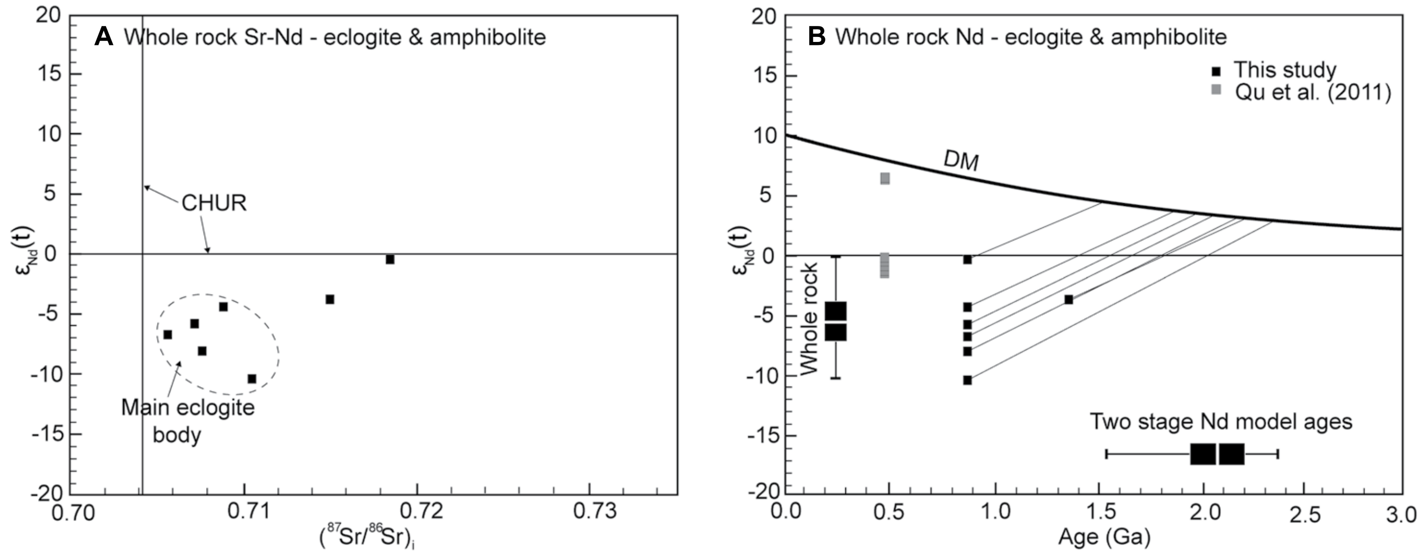

Figure 11. (A) Whole-rock ε_{Nd}(t) versus initial $^{87}Sr/^{86}Sr$ plot for the Gubaoquan area, NW China, eclogite and amphibolite. (B) Nd isotopic evolution diagram for eclogite and amphibolite samples. Depleted mantle curve is after DePaolo (1988). Black squares correspond to samples from this study and gray squares correspond to samples from Qu et al. (2011). The results from this study are given in the form of box-plots. The line across the box represents the median value of the data and ranges are the interquartile ranges (differences between third and first quartile, Q3–Q1). Dots are analysis points beyond whiskers (outliers). The number of analyses are marked. CHUR—chondritic uniform reservoir; DM—depleted mantle.

to xenomorphic with sizes of 30–90 µm (Fig. DR2). The grain in matrix is xenomorphic and 80 µm in size, with irregular shape and notable fractures. The monazite in garnet has a complex compositional zoning with an embayment in its core, which tends to be rich in U and T and poor in Y (Fig. DR2). Eight spots in monazite included in garnet or in the matrix yield $^{238}U/^{206}Pb$ ages ranging from 1190 ± 19 Ma to 807 ± 11 Ma (Figs. 12C and 12D; Table DR4). All spots have negative Eu anomalies (Eu/Eu* = 0.38–0.50; Fig. 13; Table DR5) and show type I patterns with HREE depletion and high HREE concentrations.

Metagreywacke 16JS87

In metagreywacke 16JS87, ten monazite grains (10–120 µm) included in garnet and biotite or occurring in the matrix or quartz layers were chosen for geochronological study. The monazite grains are mostly subhedral to xenomorphic with few rounded shapes (Fig. DR2). Monazite included in garnet has homogeneous composition in U and Th with very low Y content. Monazite in quartz layer and in biotite has complex zoning characterized by irregular domains rich in Y and Th and poor in U (Fig. DR2). Thirty three spots on the ten analyzed monazite grains yield a continuum of $^{238}U/^{206}Pb$ ages from 1120 ± 13 Ma to 795 ± 13 Ma (Fig. 12E; Table DR4). Ten concordant spots yield a weighted mean $^{238}U/^{206}Pb$ age of 880.7 ± 7.9 Ma (Fig. 12F). REE in all analyzed spots also show two different types of patterns: spots with type I patterns have higher HREE concentrations compared to type II spots (Fig. 13). All the analyzed spots from type I and type II display a deep negative Eu anomaly (Eu/Eu* = 0.01–0.32; Fig. 13; Table DR5).

MONAZITE AGES AND COMPOSITIONAL CHARACTERISTICS

The Meso- to Neoproterozoic inherited monazite from the metagreywackes have crystallization age ranges (1190–795 Ma) and age peak (ca. 881 Ma; Fig. 12) compatible not only with zircon crystallization ages of the eclogite and orthogneiss but also with metamorphic ages from the amphibolite. Detrital monazite surviving metamorphism have been reported only in a few locations worldwide (e.g., Williams, 2001; Rubatto et al., 2001; Daniel and Pyle, 2006; Krenn et al., 2008; Rasmussen and Muhling, 2009; Liu and Massonne, 2019). Krenn et al. (2008) pointed out that inherited monazite has generally lower Th contents and higher Y contents than metamorphic monazite. However, Y contents in monazite from this study are lower than in Paleozoic metamorphic grains from the same samples (P. Štípská personal commun., 2019), inconsistent with a detrital origin of late Mesoproterozoic to Neoproterozoic monazite (Table DR5). Inherited monazite REE distribution and trend of the Yb/Gd ratios in the Yb/Gd versus age diagram suggest existence of two types of monazites (Fig. 13D). Type I monazite grains have high HREE concentrations, high Yb/Gd ratios, and are dominated by Mesoproterozoic ages (Fig. 13D). Type II monazite grains have lower HREE concentrations, lower Yb/Gd ratios, and are exclusively characterized by Neoproterozoic ages with mean age of formation of 880.7 ± 7.9 Ma (Figs. 12F and 13D). The decrease in HREE from Mesoproterozoic type I grains to Neoproterozoic type II grains is similar to compositional characteristics of metamorphic monazite described in Rubatto et al. (2013). These authors interpreted decrease of HREE as a result of monazite crystallization with garnet growth. Moreover, the rather long crystallization time of the type I monazite would imply a long-lived metamorphic event and garnet stability in the protolith of metagreywacke. Even though accretionary processes have already been described in the south of the CAOB (i.e., Ge et al., 2014), we consider this age span as too long to represent accretionary processes. Instead, we infer that type II monazite grain crystallized together with garnet, which suggests the existence of a Neoproterozoic metamorphic event recorded in the metagreywacke at ca. 881 Ma.

DISCUSSION

In order to evaluate the petrogenesis of metabasites, orthogneisses, and metasediments we discuss first the mobility of major and trace

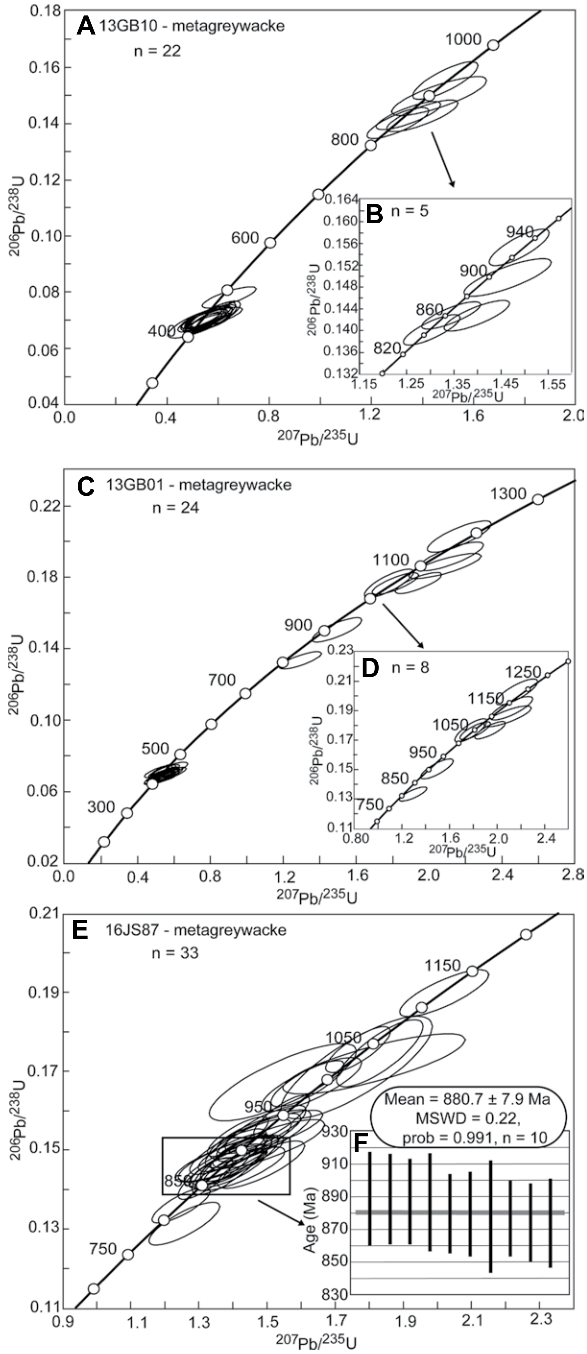

Figure 12. Concordia diagrams and $^{206}Pb/^{238}U$ weighted average age plots of monazite from metagreywacke samples 13GB10 (A, B), 13GB01 (C, D), and 16JS87 (E, F). Error ellipses and error bars are 2σ in the concordia diagrams. See text for details. CHUR—chondritic uniform reservoir; DM—depleted mantle.

elements during metamorphism. Subsequently, petrogenetic models of the Gubaoquan eclogite and amphibolite, orthogneiss and metasediments are critically debated. Finally, these petrogenetic models are integrated in a new geodynamic scenario.

Major and Trace Element Mobility during Metamorphism

Element mobilities of subducted oceanic crust during HP metamorphism has been widely investigated (e.g., Bebout et al., 1999; Rubatto and Hermann, 2003; Spandler et al., 2004, 2007; Manning, 2004; Kessel et al., 2005). Based on a compositional comparison between HP metamorphic rocks and their estimated protoliths, previous researchers proposed that LILE (Sr, K, Rb, Ba, and U) were highly mobile and could be removed from mafic rocks during eclogite-facies metamorphism (Arculus et al., 1999; Becker et al., 2000). However, a comparative study on metamorphosed oceanic crust and equivalent igneous rocks from western New Caledonia demonstrated that HP metamorphism (~1.9 GPa, ~600 °C) produces only minor changes in the composition of the rocks, and the geochemical characteristics of the rocks as well as those imposed by seafloor hydrothermal alteration can well be preserved, indicating that significant amounts of fluid-mobile elements are largely retained during the dehydration of the subducted oceanic crust at the blueschist to eclogite-facies transition (Spandler et al., 2004). Although HP metamorphism causes only limited impact on composition of subducted oceanic crust, aqueous fluids and hydrous melts in HP and ultrahigh pressure (UHP) conditions are capable of mobilizing LILE and LREE (Rubatto and Hermann, 2003; Kessel et al., 2005; Hermann et al., 2006; Zhao et al., 2007). Aqueous fluids are generally sourced from dehydration or breakdown of minerals during prograde or peak metamorphism (Zhao et al., 2007; Spandler et al., 2011), but combined evidence from experiments and natural rocks indicates that aqueous fluids liberated at the blueschist to eclogite-facies transition are dilute and contain only moderate amounts of LILE, Sr and Pb and do not transport significant amounts of key trace elements such as LREE, U and Th (Manning, 2004; Hermann et al., 2006), and HREE and HFSE are generally immobile during HP metamorphism (Zhao et al., 2007; Zheng et al., 2011). In addition, detailed petrographic and geochemical study on HP veins within UHP eclogite has shown that aqueous fluids or melts are usually channelized during HP-UHP metamorphism and their disturbance to rock composition is mainly concentrated around the areas where the channel fluids or melts flow through (Spandler et al., 2011; Guo et al., 2012). This makes it possible to avoid influence of metamorphic fluids or melts by choosing samples without HP veins.

During metamorphism, trace elements in subducted sediments have geochemical behaviors similar to those in subducted oceanic crust. In situ analyses on trapped fluid inclusions from hydrothermal piston-cylinder experiments (under H_2O saturated conditions, 2.2 GPa, and 600–750 °C) indicated that the fluids are too dilute to significantly alter the trace element content of the subducting sediments although subsolidus hydrous fluids released from subducted sediments during subduction-zone metamorphism up to eclogite-facies have relatively high LILE contents compared to REE and HFSE (Spandler et al., 2007).

There are no HP veins indicative of HP hydrothermal fluids in the studied eclogite lenses. However, felsic veins crosscutting the main eclogite body and the surrounding orthogneiss have been observed (Figs. 3A and 3B). There is no evidence of Paleozoic anatectic events af-

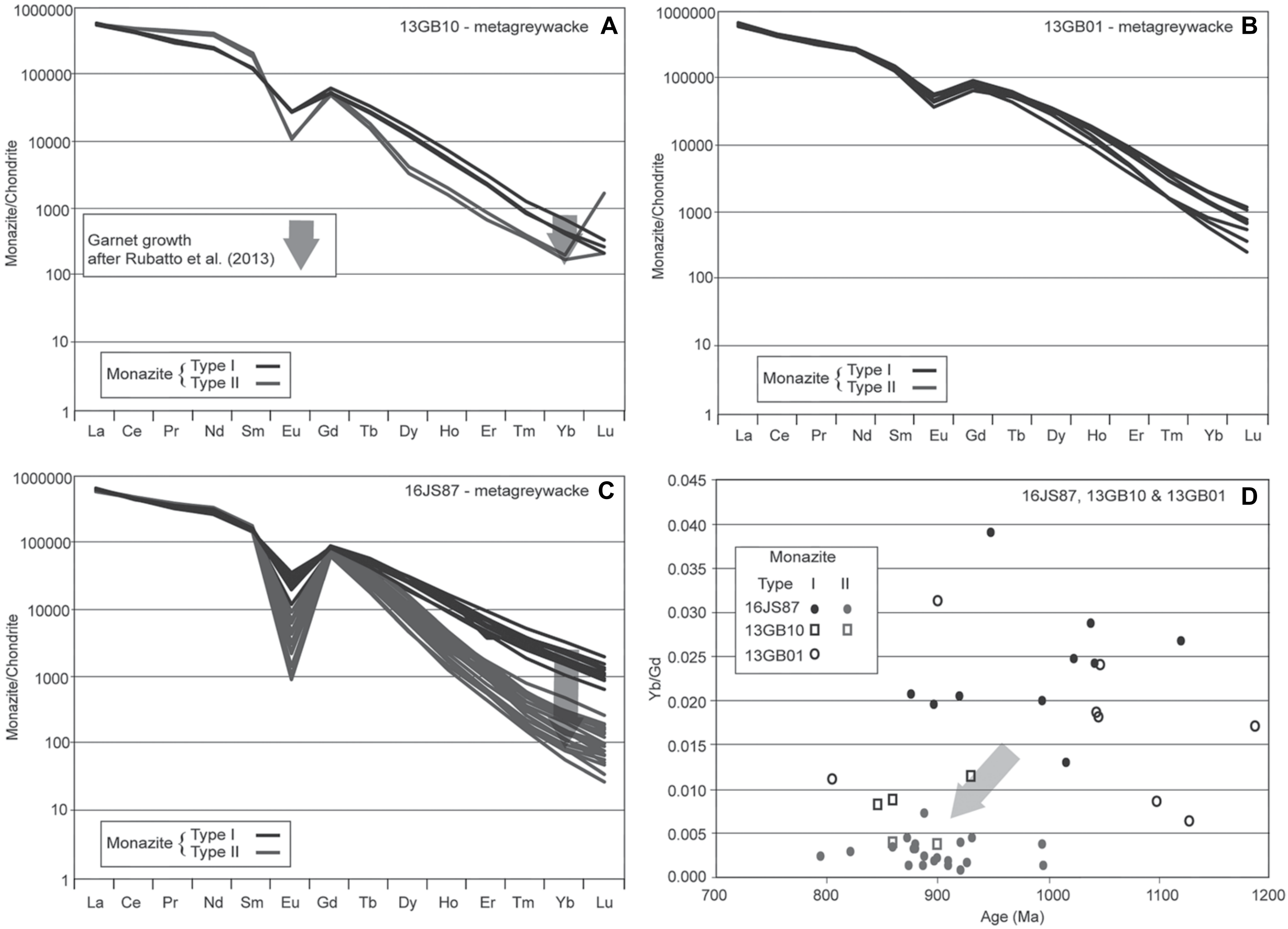

Figure 13. Chondrite-normalized rare earth element (REE) patterns of Group I and Group II inherited monazite in metagreywacke samples (A) 13GB10, (B) 13GB01, and (C) 16JS87. Shown are monazite chondrite-normalized REE patterns from Rubatto et al. (2013; dark and light gray). (D) Yb/Gd versus age diagram for inherited monazite in metagreywacke samples 13GB10, 13GB01, and 16JS87. Normalizing values are from Sun and McDonough (1989). See text for details. Grt—garnet; Mnz—monazite.

fecting eclogite, orthogneiss or metasediments and the boundary between the eclogite and felsic veins are generally clear, indicating limited material exchange between them. In addition, the eclogitic samples were collected far away from these veins to avoid potential contamination by the felsic melts. In fact, among the meta-mafic rocks, most samples exhibit basaltic composition, and their nomenclature based on TAS diagram is consistent with that achieved by immobile element based Zr/TiO_2 versus Nb/Yb diagram (Figs. 4A and 4C), confirming a limited mobilization of the alkali elements during metamorphism. Furthermore, there is no significant LILE (e.g., Cs, Rb, Ba, U) or LREE depletion in eclogite, amphibolite, orthogneiss or metasediments, and LILE and LREE elements for each rock type generally show consistent patterns (Figs. 4 and 7), indicating that trace element mobilization during partial melting or interaction with high flux fluid are insignificant (John et al., 2008). In addition, most eclogite, amphibolite, orthogneiss, and metasediment samples have loss on ignition values lower than 2.27 wt%, suggesting minor hydration or carbonation during interaction with low temperature hydrothermal fluids. The absence of major alteration in eclogite and amphibolite sample is also supported by Ce contents (Polat and Hofmann, 2003), which are consistent for all the samples except for the sample 16JS98. However, one eclogitic sample (XIGB04) has relatively evolved major element composition but abnormally low LREE contents (Table 1; Fig. 4), suggesting that the LREE of the sample might be mobilized during the eclogite-facies metamorphism. Therefore, to avoid potential disturbances on trace element system by metamorphism, immobile element based diagrams were preferably used to decipher the genesis and tectonic background of the metabasites and metagraywackes.

Petrogenesis of the Gubaoquan Eclogite and Amphibolite

A striking characteristics of the eclogite with basaltic composition is their negative Zr-Hf anomalies, which commonly exist in subduction-related basalts (e.g., Elliott et al., 1997; Rubatto and Hermann, 2003; Savov et al., 2006; Utsunomiya et al., 2011; Holm et al., 2016), but are rarely observed in oceanic MORB-type tholeiites (e.g., Arevalo and McDonough, 2010; Jenner and O'Neill, 2012). Correspondingly, such a feature can be present in arc/back-arc basalt-derived eclogites (Zhang et al., 2008; Zhang et al., 2016). Besides, some continent-derived eclogites may also show negative Zr-Hf anomalies (e.g., Zhao et al., 2007; Tang et al., 2007; Wang et al., 2013), distinct from the case of oceanic crust-derived eclogites (e.g., Zhang et al., 2005).

In the present study, Group I eclogite and amphibolite samples plot in the basaltic field in both the TAS (Le Bas et al. 1986) and the Zr/TiO_2 versus Nb/Y diagrams (Fig. 4B), and their REE distribution patterns range from typical E-MORB to N-MORB, indicating a basaltic origin for the samples from the main eclogite body (Fig. 4D). Group II eclogite and amphibolite are characterized by distinct REE and trace element distribution patterns (Figs. 4F and 4G). The Group II amphibolite sample is enriched in LREEs and is of andesitic origin. The Group II eclogite originates from the main eclogite body and its LREE distribution has been disturbed seriously. Its andesitic composition is interpreted as a probable consequence of chemical interaction with the wall-rock during metamorphism.

Available data show that most of the eclogitic rocks exhibit relative Zr-Hf depletion as indicated by their relatively low Zr/Sm ratios (Table 1; Fig. 4E), suggesting that an origin of MORB-type oceanic floor basalt is unlikely for these rocks. In addition, our U-Pb dating of zircon cores yielded a protolith age of 889.3 ± 4.8 Ma, which is consistent with the protolith ages obtained previously (Liu et al., 2011; Qu et al., 2011; Saktura et al., 2017). Because of the large time span (>400 Ma) between the formation of the protolith and its hypothetical subduction, an oceanic origin for the metabasites is unlikely. Furthermore, the occurrence of older Mesoproterozoic zircon cores precludes an oceanic origin of the eclogite.

The metabasalt samples have Nb (4.22–9.78 ppm) contents considerably higher than those of intra-oceanic arc and back-arc basalts (e.g., Hochstaedter et al., 2000; Tollstrup et al., 2010; Tamura et al., 2011), and the eclogitic metabasalt samples have Zr/Nb ratios even lower than the OIB (Zr/Nb = 5.8), suggesting a quite enriched mantle source as commonly manifested by back-arc basalts in continental margins (e.g., Espanon et al., 2014; Shuto et al., 2015). A comprehensive investigation for the geochemical trend of basalt from the NE Japan arc has revealed that there is a decreasing trend in incompatible element ratios (e.g., Nb/Yb) with age (Shuto et al., 2015), reflecting an increasing depletion of HFSE with melt extraction. The metabasalts have relatively high Nb/Yb ratios (2.3–4.8) and Zr-Hf troughs that are similar to those of early stage back-arc basalts in the NE Japan and continental rift zones (Fig. 4F; Table DR1; Shuto et al., 2015). The metabasalts have $(Nb/La)_N$ ratios (1.06–5.75) significantly higher than those of the MORB and OIB (Sun and McDonough, 1989), suggesting a contribution from asthenospheric mantle. In comparison with typical continental back-arc basalts that commonly have positive $\varepsilon_{Nd}(t)$ values (Jacques et al., 2013; Shuto et al., 2015), eclogite and amphibolite from the Beishan Orogen are dominated by negative $\varepsilon_{Nd}(t)$ values (–0.2 to –10.3; this study), suggesting that there must have been an enriched mantle component that has contributed to the genesis of the protolith of the metabasalts. A candidate for the enriched mantle component is a metasomatized lithospheric mantle characterized by less radiogenic Nd isotope composition. Lithospheric mantle can commonly contribute to the genesis of continental back-arc and rift magmatism (e.g., Jacques et al., 2013; Shuto et al., 2015). Although no coeval basalts of lithospheric mantle origin has been reported in the region, the relatively high Nb contents, low Zr/Nb ratios and the variable and mostly negative whole-rock $\varepsilon_{Nd}(t)$ and zircon $\varepsilon_{Hf}(t)$ values suggest that both the asthenospheric and lithospheric mantle components must have contributed to the genesis of the protolith of the metabasalts.

Melting of the Metasediments and Origin of the Granitic Rocks

Despite numerous geological processes during sediment transport and post-depositional diagenesis which can affect the chemical composition of sedimentary rocks, geochemical tools have been proved useful in deciphering the origin of sedimentary rocks and weathering processes (e.g., Nesbitt and Young, 1984; Taylor and McLennan, 1985; Fedo et al., 1995; Cox et al., 1995). The index of compositional variability (ICV) is defined to trace the source rocks and provenance of sediment (Nesbitt and Young, 1982; Cox et al., 1995). The metasediments in this study all have high ICV values (1.04–1.70), suggesting that they originated from an immature source and were deposited in an active margin setting (Fig. 5A). Th and Sc are relatively enriched in silicic and mafic rocks, respectively, and are usually used to trace the provenance nature of the sediments (McLennan et al. 1993; Cullers, 1994). In the Th/Sc versus Zr/Sc diagram, the metasediments have a wide range of Th/Sc ratios (0.02–7.57) and a rather consistent Zr/Sc ratios (1.04–1.70) thereby indicating a heterogeneous source composition (Fig. 5C). The slight spoon-shaped REE distribution pattern of Group C metasediments with MREE fractionation by garnet (e.g., Davidson et al., 2012) confirms the existence of multiple source rocks of metasediments (Fig. 7E).

In the La/Th versus Hf diagram, a number of the samples have felsic arc source and form a trend toward a mixed felsic/basic source with other samples (Fig. 14A). The negative Eu

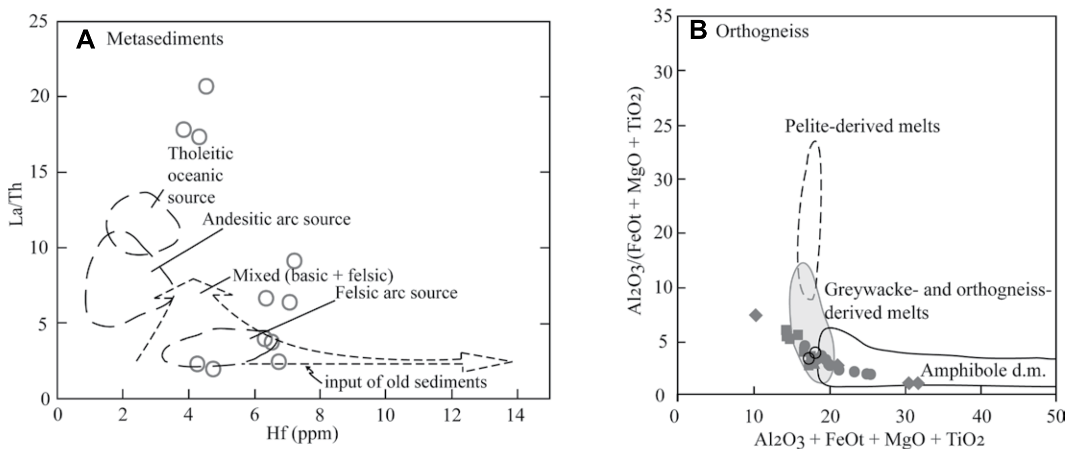

Figure 14. Geotectonic and source rock discrimination diagrams for the Gubaoquan metasediments, NW China: (A) Hf versus La/Th diagram after Floyd and Leveridge (1987). (B) Binary plot Al_2O_3 + FeOt + MgO + TiO_2 versus Al_2O_3/(FeOt + MgO + TiO_2) for orthogneiss. Outlined are domains occupied by experimental granitic melts obtained by partial melting of metapelites, metagreywackes, and amphibolites (Janoušek et al., 2010, and references therein). Shown are the plots for the orthogneiss from the Beishan Orogen from Liu et al. (2015), Yuan et al. (2015), Jiang et al. (2013), and Ye et al. (2013). d.m.—derived melts.

anomalies of Group A and Group B metasediments ($Eu/Eu^* = 0.53–0.82$) indicate that they are derived from materials which underwent feldspar fractionation.

Metagreywacke from magmatic arc, craton interiors or recycled orogens are characterized by progressively increasing La, Ce, Th, U, Hf, and REE contents as well as $(La/Yb)_N$ ratios (Bahtia, 1983, 1985). The metagreywacke samples display low to moderate La, Ce, Th, U, and Hf contents similar to those of greywackes from active continental margins or continental arcs (Table 2). Such a tectonic setting can be illustrated in the K_2O/Na_2O versus SiO_2 discrimination diagram (Roser and Korsch, 1986; Bhatia and Crook, 1986; Fig. DR3A [footnote 1]), the La-Th-Sc and Th-Sc-Zr/10 diagrams and the La/Y versus Sc/Cr diagram (Bhatia and Crook, 1986; Figs. DR3B and DR3C) where the majority of samples plot in the continental arc or the active continental margin fields. The orthogneiss samples show incompatible trace element patterns similar to those of Group A and Group B metasediments, suggesting that the metasediments were either derived from orthogneiss or that the orthogneiss was the melting product of the sedimentary package. The orthogneiss crystallized at ca. 867 Ma (Fig. 10A) whereas detrital zircons in metagreywacke display Mesoproterozoic to Neoproterozoic ages and old crustal components involved in the formation of their Mesoproterozoic source rock (upper intercept at 1461 ± 44 Ma; Fig. 10H). Thus, we infer that metasediments represent the source rock of the orthogneiss. The binary plot $Al_2O_3 + FeOt + MgO + TiO_2$ versus Al_2O_3 /$(FeOt + MgO + TiO_2)$ proved useful in discriminating the possible sources of granites (Jung et al., 2009; Janoušek et al., 2010). The orthogneiss samples plot in the fields of melts derived from quartzo-feldspathic sources such as greywacke or orthogneiss (Fig. 14B). Because of the similarity in age between the basalt (eclogite) in an extensional back-arc setting and the granitoids (orthogneiss) formed by partial melting of the greywackes, we infer that both the metabasalt and metagranitoid were formed in a similar tectonic setting. The high thermal regime required for crustal melting ca. 870 Ma is compatible with the existence of asthenospheric upwelling and back-arc opening deduced from the petrogenesis of the basaltic protolith of the eclogite and amphibolite. This Neoproterozoic thermal event is also in agreement with different metamorphic ages from zircons in the amphibolite (sample 16JS98; ca. 911 Ma) and the metagreywacke (sample 13GB01; ca. 846 Ma; Fig. 10F) as well as from the in situ ages obtained from monazite (sample 16JS87; ca. 881 Ma; Fig. 12F).

Mesoproterozoic to Neoproterozoic Tectonic Evolution of the Beishan Orogen

The new data provided in this paper allow to reconstruct the Proterozoic evolution of the Beishan Orogen in three main stages: (1) formation of the continent around 1.6 Ga, (2) inception of the subduction of the Neoproterozoic ca. 1

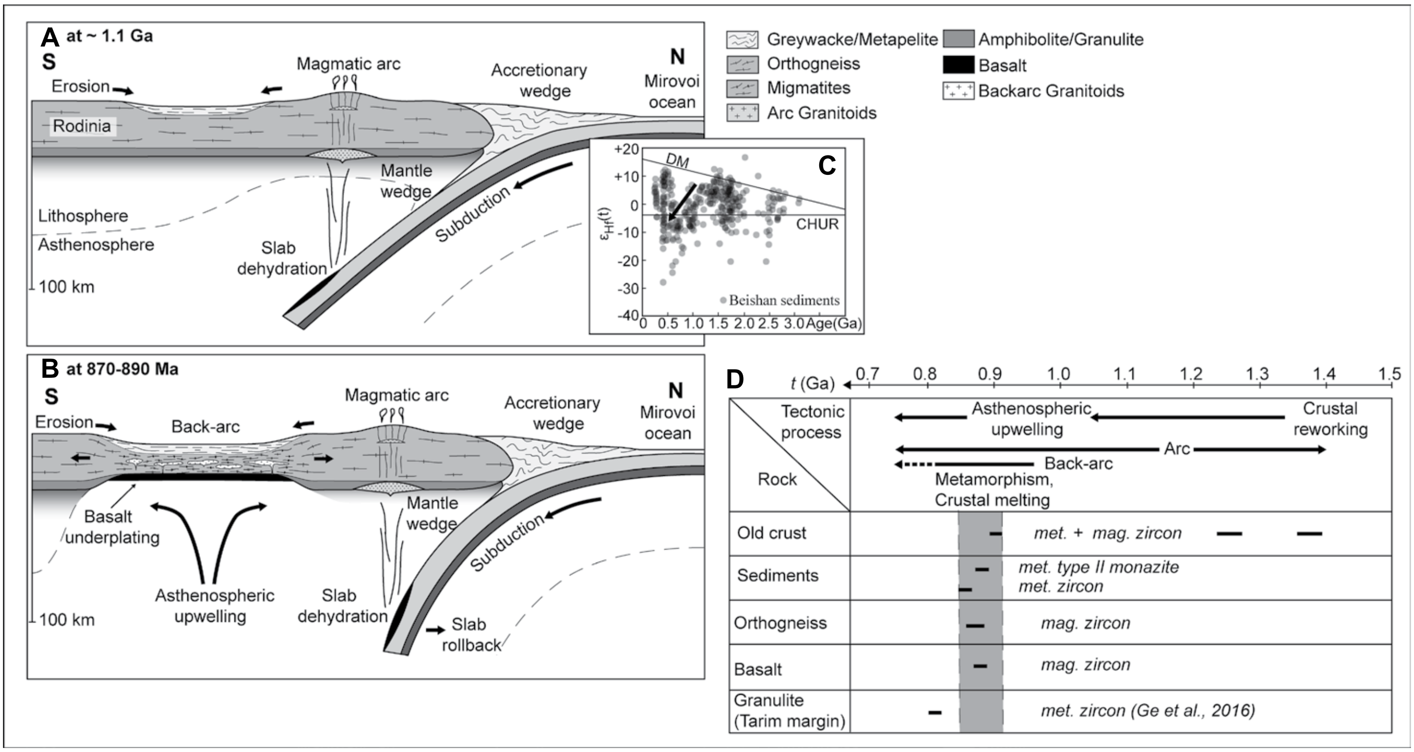

Figure 15. Evolutionary tectonic model proposed for the Beishan Orogen, NW China: (A) Shematic profile of the Mirovoi oceanic lithosphere beneath the Rodinia supercontinent during the late Mesoproterozoic. (B) Shematic profile of the Mirovoi oceanic lithosphere beneath the Rodinia supercontinent with asthenospheric upwelling, back-arc opening and high-temperature metamorphism during the Neoproterozoic. (C) Diagram of $\varepsilon_{Hf}(t)$ values versus age (Ma) for zircon from metasediments from the Beishan Orogen, plotted data from Liu et al. (2015), Song et al. (2013a, 2013b) and Song et al. (2016). (D) Geological history of the Beishan Orogen from Mesoproterozoic to Neoproterozoic. Duration of thermal and tectono-metamorphic events related to crustal reworking, arc formation, asthenospheric upwelling and back-arc opening are shown by black thick lines. Metamorphism and crustal melting events are shown in gray. Dashed black lines correspond to the uncertain existence of events. Granulite metamorphism in the northern Tarim margin is from Ge et al. (2016). CHUR—chondritic uniform reservoir; DM—depleted mantle; mag.—magmatic; met.—metamorphic.

Ga Peri-Rodinian Mirovoi Ocean (e.g., Cawood, 2005) and development of active margin Rodinian sequences, and (3) supra-subduction asthenospheric upwelling related to rollback of the subducting slab. The two staged geodynamic scenario is summarized in Figure 15.

The Rodinia continental basement in the studied area was formed at ca. 1.6–1.4 Ga as documented by ages of orthogneiss in He et al. (2018b) and Yuan et al. (2019) and detrital zircons in metasediments (Song et al., 2013a, 2013b; Liu et al., 2015, Zong et al., 2017). Negative $\varepsilon_{Hf}(t)$ values in detrital zircons and T_{DM} model ages up to 2.0 Ga indicate a significantly older continental source (Fig. 15C; Liu et al., 2015). The first late Mesoproterozoic to early Neoproterozoic event in the studied area is marked by deposition of greywackes containing zircons with U-Pb ages ranging from 1035 Ma to 871 Ma (Liu et al., 2015; Song et al., 2016; Zong et al., 2017). These zircons show either positive or weakly negative $\varepsilon_{Hf}(t)$ values (Fig. 15C) and T_{DM} model ages ranging from 1.1 to 1.9 Ga, which, together with chemistry of the sediments (Fig. 14), suggest an active margin setting of deposition typical either for accretionary wedge (Jiang et al., 2016) or back-arc (Collins, 2002; Collins and Richards, 2008). This scenario is portrayed in Figure 15A, which shows formation of an early arc system, developed on continental crust during inception of subduction of the Peri-Rodinian oceanic lithosphere.

The second Neoproterozoic event is associated with a thermal anomaly that affected the previously formed lithospheric sequence. This event is constrained by the HT metamorphism of metagreywacke (13GB10, 13GB01, and 16JS87) as shown by in situ monazite dating at ca. 881 Ma and by metamorphism of continental metabasites as shown by zircon rims U-Pb dating in amphibolite (sample 16JS98) at ca. 910 Ma. This event was followed by emplacement of granitoids in metasediments at ca. 867 Ma as documented by zircon crystallization ages of the orthogneiss (sample 16JS78) and lasted until ca. 846 Ma as shown by zircon metamorphic ages in metagreywackes (sample 13GB01). Importantly, the metamorphic and magmatic event was closely associated with the formation of the basaltic protolith of the eclogite at ca. 889 Ma (sample 17JS102), which is interpreted here in terms of crystallization of asthenospheric melt associated with elevation of mantle isotherms. This was caused by upwelling of asthenosphere that gave rise to the generation of hot basaltic magma underneath the thinned subcontinental mantle lithosphere (Fig. 15B). Crystallization of the underplated basalt released heat which resulted in partial melting of the continental crust and of the sedimentary package of the back-arc system thereby generating granitoids represented by the Beishan complex orthogneiss. These granitoids show the geochemical signature of an Andean-type arc and compositionally correspond to their sedimentary source rock (Figs. 7 and 14B) compatible with melting of the freshly deposited arc-related greywackes in an accretionary wedge or back-arc (Collins and Richards 2008; Jiang et al., 2016). Like in other accretionary systems, the granitoids left their migmatitic source and were emplaced in middle-crustal metasedimentary sequences, as in the Paleozoic accretionary wedges (Jiang et al., 2016). The long duration (ca. 1.1–0.87 Ga) of the subduction of the Mirovoi oceanic lithosphere inferred from the development of active margin Rodinian sequences in the late Mesoproterozoic–early Neoproterozoic until HT metamorphism, related to Neoproterozoic supra-subduction asthenospheric upwelling, is compatible with the duration of subduction from the end of the Mesoproterozoic until lithospheric extension leading to the break-up of Rodinia (ca. 760 Ma) suggested by paleogeographic reconstructions (e.g., Hoffman, 1991; Meert and Powell, 2001; Cawood, 2005; Cawood et al., 2016). The supra-subduction Peri-Rodinian tectonic processes probably operated during the whole period of assembly of Rodinia following the main stage of dispersal of Columbia from 1.1 Ga to 750 Ma (Zhao et al., 2018). We argue that a several hundred million year long evolution of supra-subduction systems is a typical feature of peripheral Pacific-type oceanic subduction which operated continuously from late Proterozoic to recent (e.g., Collins, 2003; Cawood et al., 2009).

The tectonic affinity of the Beishan Orogen with regards to the adjacent Tarim craton and the Central Tianshan block in the Precambrian is still debated. Based on zircon U-Pb and Hf model ages of Neoproterozoic gneisses, several researchers suggested a possible affinity between the Beishan Orogen and the Central Tianshan block (He et al., 2015; Yuan et al., 2015; Zong et al., 2017), whereas other researchers concluded that the Beishan Orogen and the Tarim shared a close peripheral position along the Rodinian margin (Liu et al., 2015). Also, the wide occurrence of 1.0–0.87 Ga magmatism in the Central Tianshan block, which is scarce in the northern margin of the Tarim craton (Shu et al., 2011; Ge et al., 2014), may indicate a similar magmatic history of the Beishan Orogen and the Central Tianshan block. Despite of the current controversies regarding the shared (e.g., Ma et al., 2012a, 2012b; Wang et al., 2014) or separated (Z.Y. Huang et al., 2015b, 2017) tectonic histories of the Central Tianshan block and the Tarim craton during the Neoproterozoic, it is generally accepted that both blocks were located at a Peri-Rodinian position in the Neoproterozoic (e.g., Ge et al., 2014; B.T. Huang et al., 2015a; Liu et al., 2015). Consequently, we discuss here the tectonic evolution of the Beishan Orogen, which is comparable to the Central Tianshan block, and the Tarim craton in the context of their mutual close Peri-Rodinian positions. The tectonic evolution presented here preceded formation of a thickened arc developed on the northern margin of the Tarim craton by at least 50 Ma (Fig. 15D) and associated HP granulite facies metamorphism (Ge et al. 2016). This 830–800 Ma crustal thickening was correlated with an advancing subduction mode of the Mirovoi oceanic lithosphere prior to the Rodinian break-up. Additionally, Zong et al. (2017) interpreted the HP granulite metamorphism at ca. 900 Ma to result from the final assembly of the Rodinia supercontinent. The geodynamic scenario presented here follows the tectonic switching model of Collins (2002) and is applicable to the modern Peri-Pacific subduction-accretionary processes governing formation of the Andes (South America) or the Cascades and the Basin and Range province (North America) (Hyndman et al., 2005). The Beishan Orogen thereby resembles most to the thinned Cascade-type continental margin with highly elevated asthenosphere and condensed thermal structure (Currie et al., 2007).

This study also shows that the Neoproterozoic tectonic processes of the northern Russian and Mongolian part of the CAOB differ substantially from those described in the Tarim-Beishan system. The Peri-Siberian domain is characterized by existence of supra-subduction arcs and back-arcs that formed from ca. 1.0 Ga to 900 Ma. This event was followed by formation of Andean-type magmatic arcs dated at 900 Ma to 760 Ma (Buriánek et al., 2017; Bold et al. 2016b; Kuzmichev and Larionov, 2011) that had been emplaced over Precambrian continental crust at 600–550 Ma. However, unlike the Peri-Siberian domains, the Beishan Orogen underwent long lasting active margin evolution starting at 1.1 Ga followed by metamorphic and magmatic events in the Neoproterozoic (910–846 Ma) related to asthenospheric upwelling and associated basaltic underplating resulting in partial melting of the continental crustal edifice (Figs. 15B and 15D). These differences between Peri-Siberian, Beishan Orogen, and adjacent areas can reflect the lateral variation of rollback dynamics or timing of inception of advancing subduction modes along-strike of the Rodinian margin. Altogether the Peri-Rodinian subduction of the Mirovoi oceanic lithosphere generated highly contrasted geodynamic processes that need to be further studied and correlated in the future.

CONCLUSIONS

(1) During late Mesoproterozoic to early Neoproterozoic the greywacke sequence was deposited coevally with formation of an early arc system developed on continental crust during subduction of the Peri-Rodinian oceanic lithosphere.

(2) The second Neoproterozoic event is due to a thermal anomaly related to asthenospheric upwelling and basaltic underplating at ca. 889 Ma that originated from an enriched mantle source probably above the retreating Peri-Rodinian subduction slab.

(3) The thermal anomaly is responsible for melting of the back-arc sedimentary package at ca. 867 Ma associated with HT metamorphism reflected by zircon rims of amphibolite (ca. 911 Ma) and monazite in metagreywacke samples (881 Ma). The HT metamorphism lasted until ca. 846 Ma as constrained by zircon metamorphic ages in metagreywackes.

ACKNOWLEDGMENTS

This research was financially supported by the National Key Research and Development Program of China (Grant no. 2017YFC0601205-2), Strategic Priority Research Program (B) of the China Academy of Sciences (XDB18020203), the National National Science Foundation of China (NSFC) projects (41573025, 41711530147), the the Czech National Grant Agency project GACR EXPRO project 17-17540S, and the Centre National de la Recherche Scientifique-NSFC project PRC1413. Schulmann Karel and Štípská Pavla acknowledge the support of the Czech National Grant Agency (GACR 19-27682X). A Guangdong Special Support Program to Jiang Yingde is acknowledged. We are grateful to Huang Zongying and Shu Chutian for their help with analytical work.

REFERENCES CITED

Arculus, R.J., Lapierre, H., and Jaillard, E., 1999, Geochemical window into subduction and accretion processes; Raspas metamorphic complex, Ecuador: Geology, v. 27, p. 547–550, https://doi.org/10.1130/0091-7613(1999)027<0547:GWISAA>2.3.CO;2.

Arevalo, J.R., and McDonough, W.F., 2010, Chemical variations and regional diversity observed in MORB: Chemical Geology, v. 271, p. 70–85, https://doi.org/10.1016/j.chemgeo.2009.12.013.

BGMRG (Bureau of Geology and Mineral Resources of Gansu Province), 1989, Regional Geology of Gansu Province: Beijing, People's Republic of China, Ministry of Geology and Mineral Resources, Geological Memoir Series 1, No. 19, Geological Publishing House, 690 p.

Bebout, G.E., Ryan, J.G., Leeman, W.P., and Bebout, A.E., 1999, Fractionation of trace elements by subduction-zone metamorphism: Effect of convergent-margin thermal evolution: Earth and Planetary Science Letters, v. 171, p. 63–81, https://doi.org/10.1016/S0012-821X(99)00135-1.

Becker, H., Jochum, K.P., and Carlson, R.W., 2000, Trace element fractionation during dehydration of eclogites from high-pressure terranes and the implications for element fluxes in subduction zones: Chemical Geology, v. 163, p. 65–99, https://doi.org/10.1016/S0009-2541(99)00071-6.

Bhatia, M.R., 1983, Plate tectonics and geochemical composition of sandstones: The Journal of Geology, v. 91, p. 611–627, https://doi.org/10.1086/628815.

Bhatia, M.R., 1985, Rare earth element geochemistry of Australian Paleozoic graywackes and mudrocks: Provenance and tectonic control: Sedimentary Geology, v. 45, p. 97–113, https://doi.org/10.1016/0037-0738(85)90025-9.

Bhatia, M.R., and Crook, K.A.W., 1986, Trace element characteristics of graywackes and tectonic setting discrimination of sedimentary basins: Contributions to Mineralogy and Petrology, v. 92, p. 181–193, https://doi.org/10.1007/BF00375292.

Bold, U., Smith, E.F., Rooney, A.D., Bowring, S.A., Buchwaldt, R., Dudás, F.Ő., Ramezani, J., Crowley, J.L., Schrag, D.P., and Macdonald, F.A., 2016a, Neoproterozoic stratigraphy of the Zavkhan terrane of Mongolia: The backbone for Cryogenian and early Ediacaran chemostratigraphic records: American Journal of Science, v. 316, p. 1–63, https://doi.org/10.2475/01.2016.01.

Bold, U., Crowley, J.L., Smith, E.F., Sambuu, O., and Macdonald, F.A., 2016b, Neoproterozoic to early Paleozoic tectonic evolution of the Zavkhan terrane of Mongolia: Implications for continental growth in the Central Asian orogenic belt: Lithosphere, v. 8, p. 729–750, https://doi.org/10.1130/L549.1.

Buriánek, D., Schulmann, K., Hrdličková, K., Hanžl, P., Janoušek, V., Gerdes, A., and Lexa, O., 2017, Geochemical and geochronological constraints on distinct Early-Neoproterozoic and Cambrian accretionary events along southern margin of the Baydrag Continent in western Mongolia: Gondwana Research, v. 47, p. 200–227, https://doi.org/10.1016/j.gr.2016.09.008.

Cawood, P.A., 2005, Terra Australis Orogen: Rodinia breakup and development of the Pacific and Iapetus margins of Gondwana during the Neoproterozoic and Paleozoic: Earth-Science Reviews, v. 69, p. 249–279, https://doi.org/10.1016/j.earscirev.2004.09.001.

Cawood, P.A., Kröner, A., Collins, W.J., Kusky, T.M., Mooney, W.D., and Windley, B.F., 2009, Accretionary orogens through Earth history, *in* Cawood, P.A., and Kröner, A., eds., Earth Accretionary Systems in Space and Time: Geological Society of London Special Publications 318, p. 1–36, https://doi.org/10.1144/SP318.1.

Cawood, P.A., Strachan, R.A., Pisarevsky, S.A., Gladkochub, D.P., and Brendan Murphy, I., 2016, Limking collisional and accretionary orogens during the Rodinia assembly and break-up: Implications for models of supercontinent cycles: Earth and Planetary Science Letters, v. 449, p. 118–126, https://doi.org/10.1016/j.epsl.2016.05.049.

Collins, W.J., 2002, Hot orogens, tectonic switching and creation of continental crust: Geology, v. 30, p. 535–538, https://doi.org/10.1130/0091-7613(2002)030<0535:HOTSAC>2.0.CO;2.

Collins, W.J., 2003, Slab pull, mantle convection, and Pangaean assembly and dispersal: Earth and Planetary Science Letters, v. 205, p. 225–237, https://doi.org/10.1016/S0012-821X(02)01043-9.

Collins, W.J., and Richards, S.W., 2008, Geodynamic significance of S-type granites in circum-Pacific orogens: Geology, v. 36, no. 7, p. 559–562, https://doi.org/10.1130/G24658A.1.

Cox, R., Lowe, D.R., and Cullers, R.L., 1995, The influence of sediment recycling and basement composition on evolution of mudrock chemistry in the southwestern United States: Geochimica et Cosmochimica Acta, v. 59, p. 2919–2940, https://doi.org/10.1016/0016-7037(95)00185-9.

Cullers, R.L., 1994, The chemical signature of source rocks in size fractions of Holocene stream sediment derived from metamorphic rocks in the Wet Mountains region, Colorado, U.S.A: Chemical Geology, v. 113, p. 327–343, https://doi.org/10.1016/0009-2541(94)90074-4.

Currie, C.A., Beaumont, C., and Huismans, R.S., 2007, The fate of subducted sediments: A case for backarc intrusion and underplating: Geology, v. 35, p. 1111–1114, https://doi.org/10.1130/G24098A.1.

Daniel, C.G., and Pyle, J., 2006, Monazite-xenotime thermochronometry and Al2SiO5 reaction textures in the Picuris range, northern New Mexico, USA: New evidence for a 1450–1400 Ma orogenic event: Journal of Petrology, v. 47, p. 97–118, https://doi.org/10.1093/petrology/egi069.

Davidson, J., Turner, S., and Plank, T., 2012, Dy/Dy*: Variations arising from mantle sources and petrogenetic processes: Journal of Petrology, v. 54, p. 527–537.

DePaolo, D.J., 1988, Neodymium Isotope Geochemistry: Berlin, Germany, Springer Verlag, 187 p., https://doi.org/10.1007/978-3-642-48916-7.

Elliott, T., Plank, T., Zindler, A., White, W., and Bourdon, B., 1997, Element transport from slab to volcanic front at the Mariana arc: Journal of Geophysical Research. Solid Earth, v. 102, p. 14991–15019, https://doi.org/10.1029/97JB00788.

Espanon, V.R., Chivas, A.R., Kinsley, L.P.J., and Dosseto, A., 2014, Geochemical variations in the Quaternary Andean back-arc volcanism, southern Mendoza, Argentina: Lithos, v. 208–209, p. 251–264, https://doi.org/10.1016/j.lithos.2014.09.010.

Fedo, C.M., Nesbitt, H.W., and Young, G.M., 1995, Unravelling the effects of Potassium metasomatism in sedimentary-rocks and paleosols, with implications for paleoweathering conditions and provenance: Geology, v. 23, p. 921–924, https://doi.org/10.1130/0091-7613(1995)023<0921:UTEOPM>2.3.CO;2.

Floyd, P.A., and Leveridge, B.E., 1987, Tectonic environment of the Devonian Gramscatho basin, south Cornwall: Framework mode and geochemical evidence from turbiditic sandstones: Journal of the Geological Society, v. 144, p. 531–542, https://doi.org/10.1144/gsjgs.144.4.0531.

Frost, B.R., Barnes, C.G., Collins, W.J., Arculus, R.J., Ellis, D.J., and Frost, C.D., 2001, A geochemical classification for granitic rocks: Journal of Petrology, v. 42, p. 2033–2048, https://doi.org/10.1093/petrology/42.11.2033.

Ge, R.F., Zhu, W.B., Wilde, S.A., He, J.V., Cui, X., Wang, X., and Zheng, B., 2014, Neoproterozoic to Paleozoic long-lived accretionary orogeny in the northern Tarim craton: Tectonics, v. 33, p. 302–329, https://doi.org/10.1002/2013TC003501.

Ge, R., Zhu, W., and Wilde, S.A., 2016, Mid-Neoproterozoic (ca. 830–800 Ma) metamorphic P-T paths link Tarim to the circum-Rodinia subduction-accretion system: Tectonics, v. 35, p. 1465–1488, https://doi.org/10.1002/2016TC004177.

Guo, S., Ye, K., Chen, Y., Liu, J., Mao, Q., and Ma, Y., 2012, Fluid-rock interaction and element mobilization in UHP metabasalt: Constraints from an omphacite-epidote vein and host eclogites in the Dabie orogen: Lithos, v. 136, p. 145–167, https://doi.org/10.1016/j.lithos.2011.11.008.

Guo, Q., Xiao, W., Hou, Q., Windley, B.F., Han, C., Tian, Z., and Song, D., 2014, Construction of Late Devonian Dundunshan arc in the Beishan orogen and its implication for tectonics of Southern Central Asian Orogenic Belt: Lithos, v. 184, p. 361–378, https://doi.org/10.1016/j.lithos.2013.11.007.

He, Z., Sun, L., Mao, L., Zong, K., and Zhang, Z., 2015, Zircon U-Pb and Hf isotopic study of gneiss and granodiorite from the southern Beishan orogenic collage: Mesoproterozoic magmatism and crustal growth: Chinese Science Bulletin, v. 60, p. 389–399, https://doi.org/10.1360/N972014-00898.

He, Z.Y., Klemd, R., Yan, L.L., Lu, T.Y., and Zhang, Z.M., 2018a, Mesoproterozoic juvenile crust in microcontinents of the Central Asian Orogenic Belt: Evidence from oxygen and hafnium isotopes in zircon: Scientific Reports, v. 8, p. 5054, https://doi.org/10.1038/s41598-018-23393-4.

He, Z.Y., Klemd, R., Li-Li Yan, L.L., and Zhang, Z.M., 2018b, The origin and crustal evolution of microcontinents in the Beishan orogen of the southern Central Asian Orogenic Belt: Earth-Science Reviews, v. 185, p. 1–14, https://doi.org/10.1016/j.earscirev.2018.05.012.

Hermann, J., Spandler, C., Hack, A., and Korsakov, A.V., 2006, Aqueous fluids and hydrous melts in high-pressure and ultra-high pressure rocks: Implications for element transfer in subduction zones: Lithos, v. 92, p. 399–417, https://doi.org/10.1016/j.lithos.2006.03.055.

Hochstaedter, A.G., Gill, J.B., Taylor, B., Ishizuka, O., Yuasa, M., and Morita, S., 2000, Across-arc geochemical trends in the Izu-Bonin arc: Constraints on source composition and mantle melting: Journal of Geophysical Research. Solid Earth, v. 105, p. 495–512, https://doi.org/10.1029/1999JB900125.

Hoffman, P.F., 1991, Did the breakout of Laurentia turn Gondwanaland inside-out?: Science, v. 252, p. 1409–1412, https://doi.org/10.1126/science.252.5011.1409.

Holm, P.M., Søager, N., Alfastsen, M., and Bertotto, G.W., 2016, Subduction zone mantle enrichment by fluids and Zr-Hf-depleted crustal melts as indicated by backarc basalts of the Southern Volcanic Zone, Argentina: Lithos, v. 262, p. 135–152, https://doi.org/10.1016/j.lithos.2016.06.029.

Hoskin, P.W.O., and Black, L.P., 2000, Metamorphic zircon formation by solid-state recrystallization of protolith igneous zircon: Journal of Metamorphic Geology, v. 18, p. 423–439, https://doi.org/10.1046/j.1525-1314.2000.00266.x.

Huang, B.T., He, Z.Y., Zhang, Z.M., Klemd, R., Zong, K.Q., and Zhao, Z.D., 2015a, Early Neoproterozoic granitic gneisses in the Chinese Eastern Tianshan: Petrogenesis and tectonic implications: Journal of Asian Earth Sciences, v. 113, p. 339–352, https://doi.org/10.1016/j.jseaes.2014.08.021.

Huang, Z.Y., Long, X.P., Kröner, A., Yuan, C., Wang, Y.J., Chen, B., and Zhang, Y.Y., 2015b, Neoproterozoic granitic gneisses in the Chinese Central Tianshan Block: Implications for tectonic affinity and Precambrian crustal evolution: Precambrian Research, v. 269, p. 73–89, https://doi.org/10.1016/j.precamres.2015.08.005.

Huang, Z.Y., Long, X.P., Wang, C.X., Zhang, Y.Y., Du, L., Yuan, C., and Xiao, W.J., 2017, Precambrian evolution of the Chinese Central Tianshan Block: Constraints on its tectonic affinity to the Tarim Craton and responses to supercontinental cycles: Precambrian Research, v. 295, p. 24–37, https://doi.org/10.1016/j.precamres.2017.04.014.

Hyndman, R.D., Currie, C.A., and Mazzotti, S.P., 2005, Subduction zone backarcs, mobile belts, and orogenic heat: GSA Today, v. 15, p. 4–10, https://doi.org/10.1130/1052-5173(2005)015<4:SZBMBA>2.0.CO;2.

Jacques, G., Hoernle, K., Gill, J., Hauff, F., Wehrmann, H., Garbe-Schönberg, D., van den Bogaard, P., Bindeman, I., and Lara, L.E., 2013, Across-arc geochemical variations in the Southern Volcanic Zone, Chile (34.5–38.0°S): Constraints on mantle wedge and slab input compositions: Geochimica et Cosmochimica Acta, v. 123, p. 218–243, https://doi.org/10.1016/j.gca.2013.05.016.

Jahn, B.M., Windley, B., Natal'in, B., and Dobretsov, N., 2004, Phanerozoic continental growth in Central Asia: Journal of Asian Earth Sciences, v. 23, p. 599–603, https://doi.org/10.1016/S1367-9120(03)00124-X.

Janoušek, V., Konopásek, J., Ulrich, S., Erban, V., Tajčmanová, L., and Jeřábek, P., 2010, Geochemical character and petrogenesis of Pan-African Amspoort suite of the Boundary Igneous Complex in the Kaoko Belt (NW Namibia): Gondwana Research, v. 18, p. 688–707, https://doi.org/10.1016/j.gr.2010.02.014.

Jenner, F.E., and O'Neill, H.St.C., 2012, Analysis of 60 elements in 616 ocean floor basaltic glasses: Geochemistry, Geophysics, Geosystems, v. 13, https://doi.org/10.1029/2011GC004009.

Jiang, H.Y., He, Z.Y., Zong, K.Q., Zhang, Z.M., and Zhao, Z.D., 2013, Zircon U-Pb dating and Hf isotopic studies on the Beishan complex in the southern Beishan orogenic belt: Yanshi Xuebao, v. 29, p. 3949–3967.

Jiang, Y.D., Schulmann, K., Sun, M., Štípská, P., Guy, A., Janoušek, V., Lexa, O., and Yuan, C., 2016, Anatexis of accretionary wedge, Pacific-type magmatism, and formation of vertically stratified continental crust in the Altai Orogenic Belt: Tectonics, v. 35, p. 3095–3118, https://doi.org/10.1002/2016TC004271.

John, T., Klemd, R., Gao, J., and Garbe-Schönberg, C.-D., 2008, Trace-element mobilization in slabs due to non steady-state fluid-rock interaction: Constraints from an eclogite-facies transport vein in blueschist (Tianshan, China): Lithos, v. 103, p. 1–24, https://doi.org/10.1016/j.lithos.2007.09.005.

Jung, S., Masberg, P., Mihm, D., and Hoernes, S., 2009, Partial melting of diverse crustal sources: Constraints from Sr-Nd-O isotope compositions of quartz diorite-granodiorite leucogranite associations (Kaoko Belt, Namibia): Lithos, v. 111, p. 236–251, https://doi.org/10.1016/j.lithos.2008.10.010.

Kessel, R., Schmidt, M.W., Ulmer, P., and Pettke, T., 2005, Trace element signature of subduction-zone fluids, melts and supercritical liquids at 120–180 km depth: Nature, v. 437, p. 724–727, https://doi.org/10.1038/nature03971.

Khain, E.V., Bibikova, E.V., Kröner, A., Zhuravlev, D.Z., Sklyaro, E.V., Fedotova, A.A., and Kravchenko-Berezhnoy, I.R., 2002, The most ancient ophiolite of the Central Asian fold belt: U-Pb and Pb-Pb evidence from the Dunzhugur complex, Eastern Sayan, Siberia, and geodynamic implications: Earth and Planetary Science Letters, v. 122, p. 329–358.

Khain, E.V., Bibikova, E.V., Sal'nikova, E.B., Kröner, A., Gibsher, A.S., Didenko, A.N., Degtyarev, K.E., and Fedotova, A.A., 2003, The Palaeo-Asian Ocean in the Neoproterozoic and early Palaeozoic, New geochronologic data and palaeotectonic reconstructions: Precambrian Research, v. 122, p. 329–358, https://doi.org/10.1016/S0301-9268(02)00218-8.

Krenn, E., Ustaszewski, K., and Finger, F., 2008, Detrital and newly formed metamorphic monazite in amphibolite-facies metapelites from the Motajica Massif, Bosnia: Chemical Geology, v. 254, p. 164–174, https://doi.org/10.1016/j.chemgeo.2008.03.012.

Kröner, A., Lehmann, J., Schulmann, K., Demoux, A., Lexa, O., Tomurhuu, D., Štípská, P., Liu, D., and Wingate, M.T.D., 2010, Lithostratigraphic and geochronological constraints on the evolution of the Central Asian Orogenic Belt in SW Mongolia: Early Paleozoic rifting followed by late Paleozoic accretion: American Journal of Science, v. 310, p. 523–574, https://doi.org/10.2475/07.2010.01.

Kuzmichev, A.B., and Larionov, A.N., 2011, The Sarkhoi Group in East Sayan: Neoproterozoic (~700–800 Ma) volcanic belt of the Andean type: Russian Geology and Geophysics, v. 52, p. 685–700, https://doi.org/10.1016/j.rgg.2011.06.001.

Kuzmichev, A.B., Bibkova, E.V., and Zhuralev, D.Z., 2001, Neoproterozoic (~800 Ma) orogeny in the Tuva-Mongolian Massif (Siberia): Island arc-continent collision at the northeast Rodinia margin: Precambrian Research, v. 110, p. 109–126, https://doi.org/10.1016/S0301-9268(01)00183-8.

Kuzmichev, A.B., Kröner, A., Hegner, E., Dunyi, L., and Yusheng, W., 2005, The Shishkhid ophiolite, northern Mongolia: A key to the reconstruction of a Neoproterozoic island-arc system in central Asia: Precambrian Research, v. 138, p. 125–150, https://doi.org/10.1016/j.precamres.2005.04.002.

Le Bas, M., Maitre, R., Streckeisen, A., and Zanettin, B., 1986, A chemical classification of volcanic rocks based on the total alkali-silica diagram: Journal of Petrology, v. 27, p. 745–750, https://doi.org/10.1093/petrology/27.3.745.

Lee, C.T.A., Leeman, W.P., Canil, D., and Li, Z.X.A., 2005, Similar V/Sc systematics in MORB and arc basalts: Implications for the oxygen fugacities of their mantle source regions: Journal of Petrology, v. 46, p. 2313–2336, https://doi.org/10.1093/petrology/egi056.

Li, S., Wang, T., Wilde, S.A., Tong, Y., Hong, D.W., and Guo, Q.Q., 2012, Geochronology, petrogenesis and tectonic implications of Triassic granitoids from Beishan, NW China: Lithos, v. 134–135, p. 123–145, https://doi.org/10.1016/j.lithos.2011.12.005.

Li, S., Wilde, S.A., and Wang, T., 2013, Early Permian post-collisional high-K granitoids from Liuyuan area in southern Beishan orogen, NW China: Petrogenesis and tectonic implications: Lithos, v. 179, p. 99–119, https://doi.org/10.1016/j.lithos.2013.08.002.

Liu, P.L., and Massonne, H.J., 2019, An anticlockwise P-T-t path at high-pressure, high-temperature conditions for a migmatitic gneiss from the island of Fjørtoft, Western Gneiss Region, Norway, indicates two burial events during the Caledonian Orogeny: Journal of Metamorphic Geology, v. 37, p. 567–588, https://doi.org/10.1111/jmg.12476.

Liu, Q., Zhao, G., Sun, M., Eizenhöfer, P.R., Han, Y., Hou, W., Zhang, X., Wang, B., Liu, D., and Xu, B., 2015, Ages and tectonic implications of Neoproterozoic ortho- and paragneisses in the Beishan Orogenic Belt, China: Precambrian Research, v. 266, p. 551–578, https://doi.org/10.1016/j.precamres.2015.05.022.

Liu, X.C., Chen, B.L., Jahn, B.M., Wu, G.G., and Liu, Y.S., 2011, Early Paleozoic (ca. 465 Ma) eclogites from Beishan (NW China) and their bearing on the tectonic evolution of the southern Central Asian Orogenic Belt: Journal of Asian Earth Sciences, v. 42, p. 715–731.

Ma, X.X., Shu, L.S., Jahn, B.M., Zhu, W.B., and Faure, M., 2012a, Precambrian tectonic evolution of Central Tianshan, NW China: Constraints from U-Pb dating and in situ Hf isotopic analysis of detrital zircons: Precambrian Research, v. 222–223, p. 450–473, https://doi.org/10.1016/j.precamres.2011.06.004.

Ma, X.X., Shu, L.S., Santosh, M., and Li, J.Y., 2012b, Detrital zircon U-Pb geochronology and Hf isotope data from Central Tianshan suggesting a link with the Tarim Block: Implications on Proterozoic supercontinent history: Precambrian Research, v. 206–207, p. 1–16, https://doi.org/10.1016/j.precamres.2012.02.015.

Maniar, P.D., and Piccoli, P.M., 1989, Tectonic discrimination of granitoids: Geological Society of America Bulletin, v. 101, p. 635–643, https://doi.org/10.1130/0016-7606(1989)101<0635:TDOG>2.3.CO;2.

Manning, C.E., 2004, The chemistry of subduction-zone fluids: Earth and Planetary Science Letters, v. 223, p. 1–16, https://doi.org/10.1016/j.epsl.2004.04.030.

Mao, Q.G., Xiao, W.J., Fang, T.H., Wang, J.B., Han, C.M., Sun, M., and Yuan, C., 2012a, Late Ordovician to early Devonian adakites and Nb-enriched basalts in the Liuyuan area, Beishan, NW China: Implications for early Paleozoic slab-melting and crustal growth in the southern Altaids: Gondwana Research, v. 22, p. 534–553, https://doi.org/10.1016/j.gr.2011.06.006.

McLennan, S.M., Hemming, S., McDaniel, D.K., and Hanson, G.N., 1993, Geochemical approaches to sedimentation, provenance, and tectonics, *in* Johnsson, M.J., and Basu, A., eds., Processes Controlling the Composition of Clastic Sediments: Geological Society of America Special Paper 284, p. 21–40, https://doi.org/10.1130/SPE284-p21.

Meert, J.G., and Powell, C.M., 2001, Assembly and break-up of Rodinia: Introduction to the special volume: Precambrian Research, v. 110, p. 1–8, https://doi.org/10.1016/S0301-9268(01)00177-2.

Mei, H., Yu, H., Li, Q., Lu, S., Li, H., Zuo, Y., Zuo, G., Ye, D., and Liu, J., 1998b, The first discovery of eclogite and Palaeoproterozoic granitoids in the Beishan area, northwestern Gansu Province, China: Chinese Science Bulletin, v. 43, p. 2105–2111.

Middlemost, E.A., 1994, Naming materials in the magma/igneous rock system: Earth-Science Reviews, v. 37, p. 215–224, https://doi.org/10.1016/0012-8252(94)90029-9.

Nesbitt, H.W., and Young, G.M., 1982, Early Proterozoic climates and plate motions inferred from major element chemistry of lutites: Nature, v. 299, p. 715–717, https://doi.org/10.1038/299715a0.

Nesbitt, H.W., and Young, G.M., 1984, Prediction of some weathering trends of plutonic and volcanic rocks based on thermodynamics and kinetic considerations: Geochimica et Cosmochimica Acta, v. 48, p. 1523–1534, https://doi.org/10.1016/0016-7037(84)90408-3.

Nie, F.J., Jiang, S.H., Bai, D.M., Wang, X.L., Su, X.X., Li, J.C., Liu, Y., and Zhao, X.M., 2002a, Metallogenic Studies and Ore Prospecting in the Conjunction Area of Inner Mongolia Autonomous Region, Gansu Province and Xinjiang Uygur Autonomous Region (Beishan Mt.), Northwest China [in Chinese with English abstract]: Beijing, China, Geological Publishing House, 408 p.

Pearce, J.A., 1996, A User's Guide to Basalt Discrimination Diagrams, *in* Wyman, D.A., ed., Trace Element Geochemistry of Volcanic Rocks: Applications for Massive Sulphide Exploration: Winnipeg, Canada, Mineral Deposits Division, Geological Association of Canada, Short Course Notes, v. 12, p. 79–113.

Pettijohn, F.J., Potter, P.E., and Siever, R., 1987, Sand and Sandstone (Second Edition): New York, New York, USA, Springer-Verlag, 553 p., https://doi.org/10.1007/978-1-4612-1066-5.

Polat, A., and Hofmann, A.W., 2003, Alteration and geochemical patterns in the 3.7–3.8 Ga Isua greenstone belt, West Greenland: Precambrian Research, v. 126, p. 197–218, https://doi.org/10.1016/S0301-9268(03)00095-0.

Qu, J.F., Xiao, W.J., Windley, B.F., Han, C.M., Mao, Q.G., Ao, S.J., and Zhang, J.E., 2011, Ordovician eclogites from the Chinese Beishan: Implications for the tectonic evolution of the southern Altaids: Journal of Metamorphic Geology, v. 29, p. 803–820, https://doi.org/10.1111/j.1525-1314.2011.00942.x.

Rasmussen, B., and Muhling, J.R., 2009, Reactions destroying detrital monazite in greenschist-facies sandstones from the Witwatersrand basin, South Africa: Chemical Geology, v. 264, p. 311–327, https://doi.org/10.1016/j.chemgeo.2009.03.017.

Ritsk, E.Y., Amelin, Y.V., Krymski, R.S., Rizvanova, N.G., and Shalaev, V.S., 1999a, The Baikal-Muya belt: Age, formation stages, and crustal evolution (U-Pb and Sm-Nd isotopic evidence) [in Russian], *in* Kariakin, Y.V., ed., Tectonics, Geodynamics, and the Processes of Magmatism and Metamorphism 2: Moscow, Russia, Geoscience Publication House, p. 93–95.

Rojas-Agramonte, Y., Kröner, A., Demoux, A., Xia, X., Wang, W., Donskaya, T., Liu, D., and Sun, M., 2011, Detrital and xenocrystic zircon ages from Neoproterozoic to Palaeozoic arc terranes of Mongolia: Significance for the origin of crustal fragments in the Central Asian Orogenic Belt: Gondwana Research, v. 19, p. 751–763, https://doi.org/10.1016/j.gr.2010.10.004.

Roser, B.P., and Korsch, R.J., 1986, Determination of tectonic setting of sandstone-mudstone suites using SiO_2 content and K_2O/Na_2O ratio: The Journal of Geology, v. 94, p. 635–650, https://doi.org/10.1086/629071.

Rubatto, D., and Hermann, J., 2003, Zircon formation during fluid circulation in eclogites (Monviso, Western Alps): Implications for Zr and Hf budget in subduction zones: Geochimica et Cosmochimica Acta, v. 67, p. 2173–2187, https://doi.org/10.1016/S0016-7037(02)01321-2.

Rubatto, D., Williams, I.S., and Buick, I.S., 2001, Zircon and monazite response to prograde metamorphism in the Reynolds Range, central Australia: Contributions to Mineralogy and Petrology, v. 140, p. 458–468, https://doi.org/10.1007/PL00007673.

Rubatto, D., Chakraborty, S., and Dasgupta, S., 2013, Time scales of crustal melting in the Higher Himalayan Crystallines (Sikkim, Eastern Himalaya) inferred from trace element-constrained monazite and zircon chronology: Contributions to Mineralogy and Petrology, v. 165, p. 349–372, https://doi.org/10.1007/s00410-012-0812-y.

Rudnick, R., and Gao, S., 2003, Composition of the continental crust, *in* Holland, H.D., and Turekian, K.K., eds., Treatise on Geochemistry: Oxford, UK, Elsevier-Pergamon, p. 1–64.

Saktura, W.M., Buckman, S., Nutman, A.P., Belousova, E.A., Yan, Z., and Aitchison, J.C., 2017, Continental origin of the Gubaoquan eclogite and implications for evolution of the Beishan Orogen, Central Asian Orogenic Belt, NW China: Lithos, v. 294–295, p. 20–38, https://doi.org/10.1016/j.lithos.2017.10.004.

Savov, I.P., Hickey-Vargas, R., D'Antonio, M., Ryan, J.G., and Spadea, P., 2006, Petrology and geochemistry of West Philippine basin basalts and early Palau-Kyushu arc volcanic clasts from ODP Leg 195, site 1201D: Implications for the early history of the Izu-Bonin-Mariana arc: Journal of Petrology, v. 47, p. 277–299, https://doi.org/10.1093/petrology/egi075.

Şengör, A.M.C., Natal'in, B.A., and Burtman, U.S., 1993, Evolution of the Altaid tectonic collage and Palaeozoic crustal growth in Eurasia: Nature, v. 364, p. 299–307, https://doi.org/10.1038/364299a0.

Shaw, D.M., 1972, The origin of the Apsley gneiss, Ontario: Canadian Journal of Earth Sciences, v. 9, p. 18–35, https://doi.org/10.1139/e72-002.

Shervais, J.W., 1982, Ti-V plots and the petrogenesis of modem and ophiolitic lavas: Earth and Planetary Science Letters, v. 59, p. 101–118, https://doi.org/10.1016/0012-821X(82)90120-0.

Shu, L.S., Deng, X.L., Zhu, W.B., Ma, D.S., and Xiao, W.J., 2011, Precambrian tectonic evolution of the Tarim Block, NW China: new geochronological insights from the Quruqtagh domain: Journal of Asian Earth Sciences, v. 42, p. 774–790, https://doi.org/10.1016/j.jseaes.2010.08.018.

Shuto, K., Nohara-Imanaka, R., Sato, M., Takahashi, T., Takazawa, E., Kawabata, H., Takanashi, K., Ban, M., Watanabe, N., and Fujibayashi, N., 2015, Across-arc variations in geochemistry of Oligocene to Quaternary basalts from the NE Japan arc: Constraints on source composition, mantle melting and slab input composition: Journal of Petrology, v. 56, p. 2257–2294, https://doi.org/10.1093/petrology/egv073.

Song, S., Su, L., Li, X., Miu, Y., and Zhang, L., 2012, Grenville-age orogenesis in the Qaidam-Qilian block: The link between South China and Tarim: Precambrian Research, v. 220, p. 9–22, https://doi.org/10.1016/j.precamres.2012.07.007.

Song, D., Xiao, W., Han, C., Li, J., Qu, J., Guo, Q., Lin, L., and Wang, Z., 2013a, Progressive accretionary tectonics of the Beishan orogenic collage, southern Altaids: Insights from zircon U-Pb and Hf isotopic data of high-grade complexes: Precambrian Research, v. 227, p. 368–388, https://doi.org/10.1016/j.precamres.2012.06.011.

Song, D., Xiao, W., Han, C., Tian, Z., and Wang, Z., 2013b, Provenance of metasedimentary rocks from the Beishan orogenic collage, southern Altaids: Constraints from detrital zircon U-Pb and Hf isotopic data: Gondwana Research, v. 24, p. 1127–1151, https://doi.org/10.1016/j.gr.2013.02.002.

Song, D., Xiao, W., Windley, B.F., Han, C., and Yang, L., 2016, Metamorphic complexes in accretionary orogens: Insights from the Beishan collage, southern Central Asian Orogenic Belt: Tectonophysics, v. 688, p. 135–147, https://doi.org/10.1016/j.tecto.2016.09.012.

Spandler, C., Hermann, J., Arculus, R., and Mavrogenes, J., 2004, Geochemical heterogeneity and element mobility in deeply subducted oceanic crust; insights from high-pressure mafic rocks from New Caledonia: Chemical Geology, v. 206, p. 21–42, https://doi.org/10.1016/j.chemgeo.2004.01.006.

Spandler, C., Mavrogenes, J., and Hermann, J., 2007, Experimental constraints on element mobility from subducted sediments using high-P synthetic fluid/melt inclusions: Chemical Geology, v. 239, p. 228–249, https://doi.org/10.1016/j.chemgeo.2006.10.005.

Spandler, C., Pettke, T., and Rubatto, D., 2011, Internal and external fluid sources for eclogite-facies veins in the Monviso meta-ophiolite, Western Alps: Implications for fluid flow in subduction zones: Journal of Petrology, v. 52, p. 1207–1236, https://doi.org/10.1093/petrology/egr025.

Sun, S.S., and McDonough, W.F., 1989, Chemical and isotopic systematics of oceanic basalts: Implications for mantle composition and processes, *in* Saunders, A.D., and Norry, M.J., eds., Magmatism in Ocean Basins: Geological Society of London Special Publication 42, p. 313–345, https://doi.org/10.1144/GSL.SP.1989.042.01.19.

Tamura, Y., Ishizuka, O., Stern, R.J., Shukuno, H., Kawabata, H., Embley, R.W., Hirahara, Y., Chang, Q., Kimura, J.-I., Tatsumi, Y., Nunokawa, A., and Bloomer, S.H., 2011, Two primary basalt magma types from Northwest Rota-1 volcano, Mariana arc and its mantle diapir or mantle wedge plume: Journal of Petrology, v. 52, p. 1143–1183, https://doi.org/10.1093/petrology/egr022.

Tang, H.F., Liu, C.Q., Nakai, S.I., and Orihashi, Y., 2007, Geochemistry of eclogites from Dabie-Sulu terrane, eastern China: New insights into protoliths and trace element behavior during UHP metamorphism: Lithos, v. 95, p. 441–457, https://doi.org/10.1016/j.lithos.2006.09.007.

Taylor, S.R., and McLennan, S.M., 1985, The continental crust: its composition and evolution.

Tollstrup, D., Gill, J., Kent, A., Prinkey, D., Williams, R., Tamura, Y., and Ishizuka, O., 2010, Across-arc geochemical trends in the Izu-Bonin arc: Contributions from the subducting slab, revisited: Geochemistry, Geophysics, Geosystems, v. 11, no. 1, https://doi.org/10.1029/2009GC002847.

Utsunomiya, A., Jahn, B.M., Okamoto, K., Ota, T., and Shinjoe, H., 2011, Intra-oceanic island arc origin for Iratsu eclogites of the Sanbagawa belt, central Shihoku, southwest Japan: Chemical Geology, v. 280, p. 97–114, https://doi.org/10.1016/j.chemgeo.2010.11.001.

Wang, H., Wu, Y.B., Gao, S., Liu, X.C., Liu, Q., Qin, Z.W., Xie, S.W., Zhou, L., and Yang, S.H., 2013, Continental origin of eclogites in the North Qinling terrane and its tectonic implications: Precambrian Research, v. 230, p. 13–30, https://doi.org/10.1016/j.precamres.2012.12.010.

Wang, H.Y., Chen, H.X., Zhang, Q.W., Shi, M.Y., Yan, Q.R., Hou, Q.L., Zhang, Q., Kusky, T., and Wu, C.M., 2017, Tectonic mélange records the Silurian–Devonian subduction-metamorphic process of the southern Dunhuang terrane, southernmost Central Asian Orogenic Belt: Geology, v. 45, p. 427–430, https://doi.org/10.1130/G38834.1.

Wang, Z.M., Han, C.M., Xiao, W.J., Su, B.X., Sakyi, P.A., Song, D.F., and Lin, L.N., 2014, The petrogenesis and tectonic implications of the granitoid gneisses from Xingxingxia in the eastern segment of Central Tianshan: Journal of Asian Earth Sciences, v. 88, p. 277–292, https://doi.org/10.1016/j.jseaes.2014.03.015.

Whitney, D.L., and Evans, B.W., 2010, Abbreviations for names of rock-forming minerals: The American Mineralogist, v. 95, p. 185–187, https://doi.org/10.2138/am.2010.3371.

Wilhem, C., Windley, B.F., and Stampfli, G.M., 2012, The Altaids of Central Asia: a tectonic and evolutionary innovative review: Earth-Science Reviews, v. 113, p. 303–341, https://doi.org/10.1016/j.earscirev.2012.04.001.

Williams, I.S., 2001, Response of detrital zircon and monazite, and their U—Pb isotopic systems, the regional metamorphism and host-rock partial melting, Cooma Complex, southeastern Australia: Australian Journal of Earth Sciences, v. 48, p. 557–580, https://doi.org/10.1046/j.1440-0952.2001.00883.x.

Xiao, W.J., Mao, Q.G., Windley, B.F., Han, C.M., Qu, J.F., Zhang, J.E., Ao, S.J., Guo, Q.Q., Cleven, N.R., Lin, S.F., Shan, Y.H., and Li, J.L., 2010, Paleozoic multiple accretionary and collisional processes of the Beishan orogenic collage: American Journal of Science, v. 310, p. 1553–1594, https://doi.org/10.2475/10.2010.12.

Xiao, W., Windley, B.F., Han, C., Liu, W., Wan, B., Zhang, J., Ao, S., Zhang, Z., and Song, D., 2018, Late Paleozoic to early Triassic multiple roll-back and oroclinal bending of the Mongolia collage in Central Asia: Earth-Science Reviews, v. 186, p. 94–128, https://doi.org/10.1016/j.earscirev.2017.09.020.

Yang, J.S., Wu, C.L., Chen, S.Y., Shi, R.D., and Zhang, J.X., 2006, Neoproterozoic eclogitic metamorphic age of the Beishan eclogite of Gansu, China: Evidence from SHRIMP U-Pb isotope dating [in Chinese with English abstract]: Geology in China, v. 33, p. 317–325.

Ye, X.F., Zong, K.Q., Zhang, Z.M., He, Z.Y., Liu, Y.S., Hu, Z.C., and Wang, W., 2013, Geochemistry of Neoproterozoic granite in Liuyuan area of southern Beishan orogenic belt and its geological significance [in Chinese with English abstract]: Geological Bulletin of China, v. 32, p. 307–317.

Yuan, Y., Zong, K., He, Z., Klemd, R., Liu, Y., Hu, Z., Guo, J., and Zhang, Z., 2015, Geochemical and geochronological evidence for a former early Neoproterozoic microcontinent in the South Beishan Orogenic Belt, southernmost Central Asian Orogenic Belt: Precambrian Research, v. 266, p. 409–424, https://doi.org/10.1016/j.precamres.2015.05.034.

Yuan, Y., Zong, K., Cawood, P.A., Cheng, H., Yu, Y., Guo, J., Liu, Y.S., Hu, Z., and Li, M., 2019, Implication of Mesoproterozoic (~1.4 Ga) magmatism within microcontinents along the southern Central Asian Orogenic Belt: Precambrian Research, v. 327, p. 314–326, https://doi.org/10.1016/j.precamres.2019.03.014.

Zhang, G.B., Song, S.G., Zhang, L.F., and Niu, Y.L., 2008, The subducted oceanic crust within continental-type UHP metamorphic belt in the North Qaidam, NW China: Evidence from petrology, geochemistry and geochronology: Lithos, v. 104, p. 99–118, https://doi.org/10.1016/j.lithos.2007.12.001.

Zhang, L.F., Ai, Y.L., Li, Q., Li, X.P., Song, S.G., and Wei, C.J., 2005, The formation and tectonic evolution of UHP metamorphic belt in southwestern Tianshan, Xinjiang [in Chinese with English abstract]: Yanshi Xuebao, v. 21, p. 1029–1038.

Zhang, L., Chen, R.X., Zheng, Y.F., Hu, Z.C., Yang, Y.H., and Xu, L.J., 2016, Geochemical constraints on the protoliths of eclogites and blueschists from North Qilian, northern Tibet: Chemical Geology, v. 421, p. 26–43, https://doi.org/10.1016/j.chemgeo.2015.11.026.

Zhang, W., Wu, T., Zheng, R., Feng, J., Luo, H., He, Y., and Xu, C., 2012, Post-collisional Southeastern Beishan granites: Geochemistry, geochronology, Sr-Nd-Hf isotopes and their implications for tectonic evolution: Journal of Asian Earth Sciences, v. 58, p. 51–63, https://doi.org/10.1016/j.jseaes.2012.07.004.

Zhao, G.C., Wang, Y.J., Huang, B.C., Dong, Y.P., Li, S.Z., Zhang, G.W., and Yu, S., 2018, Geological reconstructions of the East Asian blocks: From the breakup of Rodinia to the assembly of Pangea: Earth-Science Reviews, v. 186, p. 262–286, https://doi.org/10.1016/j.earscirev.2018.10.003.

Zhao, Z.F., Zheng, Y.F., Chen, R.X., Xia, Q.X., and Wu, Y.B., 2007, Element mobility in mafic and felsic ultrahigh-pressure metamorphic rocks during continental collision: Geochimica et Cosmochimica Acta, v. 71, p. 5244–5266, https://doi.org/10.1016/j.gca.2007.09.009.

Zheng, R., Li, J., Xiao, W., and Zhang, J., 2018, Nature and provenance of the Beishan complex, southernmost central Asian orogenic belt: International Journal of Earth Sciences, v. 4, p. 1–27.

Zheng, Y.F., Xia, Q.X., Chen, R.X., and Gao, X.Y., 2011, Partial melting, fluid supercriticality and element mobility in ultrahigh-pressure metamorphic rocks during continental collision: Earth-Science Reviews, v. 107, p. 342–374, https://doi.org/10.1016/j.earscirev.2011.04.004.

Zonenshain, L.P., 1973, The evolution of central Asiatic geosynclines through sea-floor spreading, Tectonophysics, v. 19, p. 213–232, https://doi.org/10.1016/0040-1951(73)90020-6.

Zong, K.Q., Klemd, R., Yuan, Y., He, Z.Y., Guo, J.L., Shi, X.L., Liu, Y.S., Hu, Z.C., and Zhang, Z., 2017, The assembly of Rodinia: The correlation of early Neoproterozoic (ca. 900 Ma) high-grade metamorphism and continental arc formation in the southern Beishan Orogen, southern Central Asian Orogenic Belt (CAOB): Precambrian Research, v. 290, p. 32–48, https://doi.org/10.1016/j.precamres.2016.12.010.

Zuo, G.C., Zhang, S.L., Wang, X., Jin, S.Q., He, G.Q., Zhang, Y., Li, H.C., and Bai, W.C., 1990, Plate Tectonics and Metallogenic Regularities in Beishan Region, Peking: Beijing, University Publishing House, 226 p.

Zuo, G.C., Zhang, S.L., He, G.Q., and Zhang, Y., 1991, Plate tectonic characteristics during the early Paleozoic in Beishan near the Sino-Mongolian border region, China: Tectonophysics, v. 188, p. 385–392, https://doi.org/10.1016/0040-1951(91)90466-6.

Science Editor: Wenjiao Xiao
Associate Editor: Yongjiang Liu

Manuscript Received 26 June 2019
Revised Manuscript Received 26 September 2019
Manuscript Accepted 30 October 2019

Printed in the USA